Constitutive modelling of non-cohesive soils under high-strain rates: a consistency approach

LUIS E. ZAMBRANO-CRUZATTY*, ALBA YERRO† and JORGE MACEDO‡

Rapid loading of sands is a common issue in geotechnical engineering problems such as projectile or free-fall impact. At high strain rates (HSR), soils show more strength and enhanced dilation (viscoplastic behaviour) compared to the response at low rates (inviscid behaviour). However, few constitutive models account for the viscoplasticity of sands. Hence, the development of viscoplastic models is highly desired. Usually, viscoplasticity is modelled using overstress methods. However, overstress methods impose an overall modification of the constitutive equations, which prevents control of the evolution of internal state variables and the enforcement of the consistency condition. In this study, a generalised consistency–viscoplasticity method is proposed and applied to a non-associative modified Mohr–Coulomb model with coupled stress–dilation relation. The influence of strain rate is incorporated using a work–energy approach by way of an inertial coefficient. Two explicit integration strategies are proposed and compared, and guidelines for their implementation are shared. The numerical response of the model is tested by using drained triaxial simulations under constant axial strain rate, relaxation and impact loading. The results indicate that the consistency–viscoplasticity is a feasible alternative to simulate soil behaviour under HSR, capturing reasonably well the observed experimental responses.

KEYWORDS: consistency; constitutive relations; elasto-viscoplasticity; sands; time dependence

INTRODUCTION

Recent advancements in computational techniques to model large deformations, such as the arbitrary Lagrangian–Eulerian finite-element method (ALE) (Benson, 1989; DSS, 2012) or the material point method (MPM) (Sulsky *et al*., 1995; Al-Kafaji, 2013; Yerro Colom, 2015) have made possible the simulation of high-strain-rate (HSR) loading on large-deformation problems in geo-systems (Kim *et al*., 2015; Tran & Soowski, 2019). However, only a handful of constitutive models are available for granular materials that account for HSR effects (Liingaard *et al*., 2004; Lu & Fall, 2018).

One reason is that sand is generally hypothesised to be insensitive to rate effects. This is because sand's viscous effects are not significant at low strain rates and relatively large confinement pressures (e.g. more than one metre of overburden) (da Cruz *et al*., 2005; Hurley & Andrade, 2015). However, there is abundant evidence that for strain rates in the impact regime (e.g. free-fall or projectile impact), HSR effects are significant (Lade *et al*., 2009; Yamamuro *et al*., 2011; Omidvar *et al*., 2012; Suescun-Florez & Iskander, 2017). This is illustrated in Fig. 1, which presents the results of vacuum-dry triaxial tests conducted by Yamamuro *et al*. (2011) at different strain rates and void ratios. The effects of increasing the loading rate can be summarised as: (*a*) increased strength (Fig. 1(a)); (*b*) early manifestation of the peak stress ratio ($\eta = q/p$, with p = mean stress and q = deviatoric stress) (Fig. 1(a)); and (*c*) increased dilation and reduced contraction (Fig. 1(b)). These salient features of soil behaviour are caused by several HSR-induced micro-mechanical effects occurring at the particle level (e.g. modified trajectory of particles, inertial effects, particle breakage) (da Cruz *et al*., 2005; Yamamuro *et al*., 2011; Andrade *et al*., 2012; Omidvar *et al*., 2012; Hurley & Andrade, 2015; Suescun-Florez *et al*., 2015). Understanding the aforementioned phenomena is of critical importance, for example, for the analysis of impact and blasting problems (e.g. Higgins *et al*., 2013; Zambrano-Cruzatty & Yerro, 2020). Thus, the development of constitutive equations incorporating the effects of HSR is highly desirable, especially for the simulation of non-cohesive soils (e.g. sands).

Numerous researchers have calibrated viscoplastic constitutive models using the Yamamuro *et al*. (2011) data set (Higgins *et al*., 2013; Xu & Zhang, 2015; Mukherjee *et al*., 2020). The majority of these developments are based on phenomenological equations and are typically constructed using overstress methods such as those proposed by Perzyna (1966) and Duvaut & Lions (1976). In those methods, an explicit calculation of the viscoplastic strain (Perzyna, 1966) or the viscoplastic stress (Duvaut & Lions, 1976) is used to integrate the model. Thus, the approach eliminates the need to satisfy the consistency condition and allows stresses laid outside the yield surface; hence, the term 'overstress'. For example, Perzyna viscoplasticity requires an overstress function to explicitly calculate the viscoplastic strains ($\mathrm{d}\boldsymbol{\varepsilon}^{\mathrm{vp}}$), as shown in equation (1)

$$\mathrm{d}\boldsymbol{\varepsilon}^{\mathrm{vp}} = \langle \Phi(F) \rangle \partial F / \partial \boldsymbol{\sigma} \tag{1}$$

with F = yield function, $\Phi(F)$ = overstress function, $\partial F/\partial \boldsymbol{\sigma}$ the normal vector to the yield function, and $\langle x \rangle = x$ if $x > 0$ or 0 otherwise (being x a scalar variable). This approach adds

Manuscript received 8 July 2021; revised manuscript accepted 17 May 2022.
Discussion on this paper is welcomed by the editor.

* University of Maine, Orono, Maine, USA; also Escuela Superior Politecnica del Litoral, Guayaquil, Ecuador (Orcid:0000-0003-1699-3943).
† Virginia Tech, Blacksburg, Virginia, USA.
‡ Georgia Tech, Atlanta, Georgia, USA (Orcid:0000-0002-0457-4824).

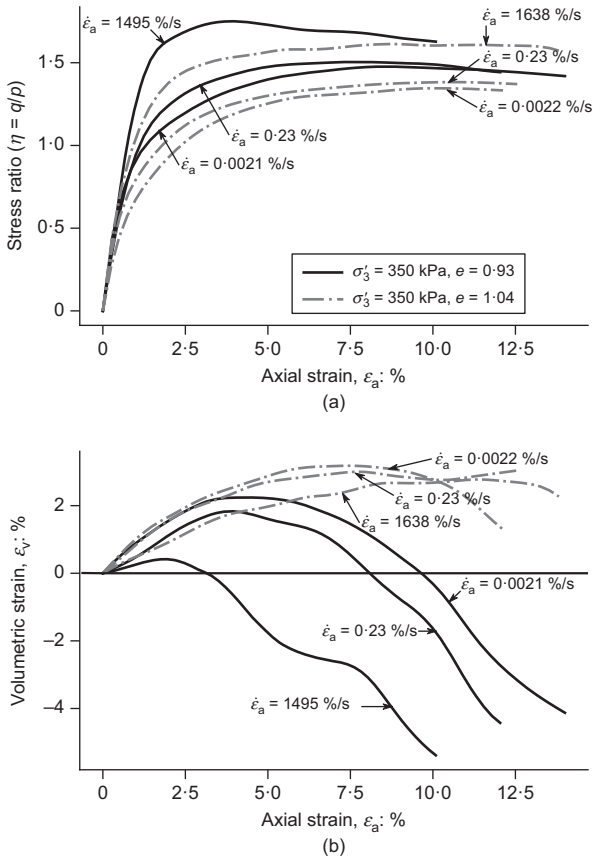

Fig. 1. Vacuum triaxial tests at σ'_3 = 350 kPa with different void ratios and rates of loading. (a) Stress ratio ($\eta = q/p$) plotted against axial strain and (b) volumetric strain plotted against axial strain. After Yamamuro *et al.* (2011)

an extra parameter that modifies the stress–strain response of the model. Overstress viscoplasticity can reproduce time-dependent behaviours, such as relaxation and creep (Katona, 1984; Wang *et al.*, 1997; Heeres *et al.*, 2002; Liingaard *et al.*, 2004; An *et al.*, 2011). However, overstress methods are not suitable for stress reversal paths (Heeres *et al.*, 2002), rendering them unsuitable for dynamic problems like earthquake loading.

An alternative method to overstress is to enforce the consistency condition using strain-rate hardening/softening equations; hence, the name 'consistency approach'. Wang *et al.* (1997) coined the term and used the consistency approach for a von Mises model with simple work-hardening and strain-rate hardening/softening laws which dynamically modify the yield loci. This dynamic change of the yield surface is the so-called 'non-stationary' yield surface, which was generalised by Olszak & Perzyna (1966). Consistent-viscoplasticity models are capable of reproducing relaxation and creep behaviour (Heeres *et al.*, 2002; Liingaard *et al.*, 2004). In addition, due to their mathematical structure, consistent-viscoplasticity models are more efficient when tracking stress reversals than overstress methods (Heeres *et al.*, 2002). However, unlike overstress methods, consistency-viscoplasticity requires extra strain-rate hardening/softening equations to describe the evolution of the model's internal state variables.

In this study, a consistent-viscoplasticity approach is proposed and is implemented on a novel and simple non-associative modified Mohr–Coulomb model (NAMC) with coupled stress–dilation. The document is organised as follows. First, the reference laboratory data set (Yamamuro *et al.*, 2011) and corresponding data-processing methods are presented. Then, the NAMC is established together with the equations governing the state variable of the model (i.e. plastic dilation D^p), which are derived using a work–energy balance approach by way of stress dilatancy and inertial effects. Following that, the generalised consistency–viscoplasticity formulation is presented in such a way that it may be applied to any inviscid elastoplastic model. Two procedures for the integration of such a framework on a given constitutive equation are presented: the first one is based on the original ideas of Wang *et al.* (1997), and the second one is a particularisation of Olszak & Perzyna (1966) for strain rates termed the 'dashpot method'. Subsequently, the experiments of Yamamuro *et al.* (2011) are replicated using the proposed viscoplastic NAMC. Furthermore, the viscoplastic NAMC is evaluated under relaxation and impact loading paths. Finally, a discussion and conclusion section, delineating the strengths, limitations and needed research, is provided.

DATA PROCESSING

As with previous studies, the data set of Yamuro *et al.* (YEA2011) (Yamamuro *et al.*, 2011) was utilised in this work to evaluate the behaviour of sands under different strain rates. It consists of 14 triaxial tests performed on precrushed coral sand with specific gravity of 2·68 and void ratios ranging from 1·20 to 0·74. It is classified as poorly graded sand (SP) according to the Unified Soil Classification System (Howard, 1984). Yamamuro *et al.* (2011) presented results of vacuum-dry drained triaxial tests, which prevented any generation of air pore pressure. Strain rates ranging between 0·0022%/s and 1764%/s were reached with a free-fall weight that pushed an axial piston to shear the samples. Two confinement pressures of 98 kPa and 350 kPa were applied to sand samples having initial void ratios of 0·93 and 1·04.

For the purpose of this work, the data set was manually digitised and a Savitzky–Golay filter (Savitzky & Golay, 1964) was utilised to denoise the filtered data (Klotz & Coop, 2002; Jefferies *et al.*, 2015). The filtering process permitted the rendering of consistent relationships between the deviator stress (σ_d), the volumetric strain (ε_v) and the axial strain (ε_a). A filtered data set displayed in Fig. 2 demonstrates the consistency of the original and filtered data. It is important to note that the YEA2011 data set has some limitations due to the nature of HSR triaxial tests. One concern is that global strain measurements contain significant oscillations due to wave propagation, as described in Abrantes & Yamamuro (2002). For this reason, the strains were measured locally, on a disc of 1·25 cm positioned at the specimen's mid-height, as it appeared to filter out the strain oscillations (Abrantes & Yamamuro, 2002). As will be shown in further sections, few oscillations persisted, particularly for HSR (e.g. test with $\dot{\varepsilon}_a = 1495\%/s$ in Fig. 1(b)), which makes the dilation calculation ($d\varepsilon_v/d\varepsilon_q$ with ε_q the deviatoric strain) relatively challenging. Moreover, in local strains, dilation and contraction are enhanced compared to the global ones (Abrantes & Yamamuro, 2002; Klotz & Coop, 2002). Therefore, to partially correct these distortions, the local strains are adjusted according to the approach detailed in Klotz & Coop (2002), with the steps for this adjustment explained in detail in Zambrano-Cruzatty (2021).

VISCOPLASTIC NON-ASSOCIATIVE MODIFIED MOHR–COULOMB

This section proposes a non-associative viscoplastic model based on the Mohr–Coulomb formulation. The objective of this exercise is to develop a straightforward and robust model that fundamentally combines friction and dilatation. While the standard Mohr–Coulomb model has disassociated

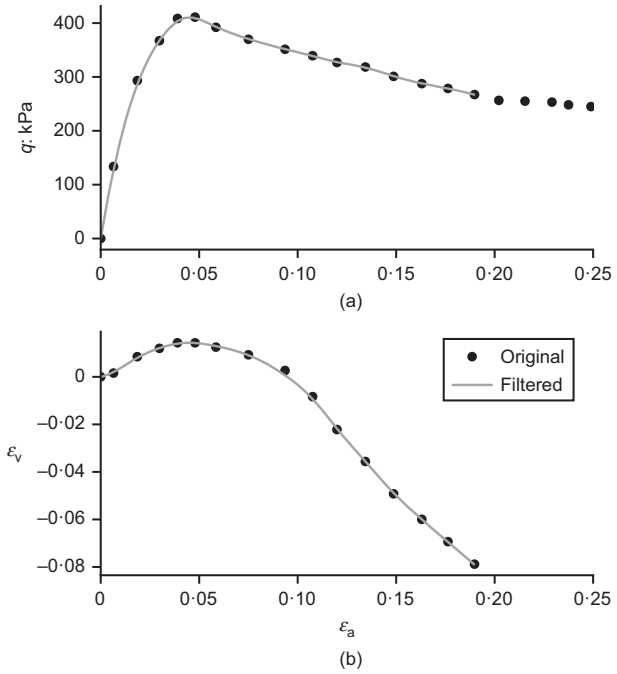

Fig. 2. Comparison between the original digitised data (points) and the filtered triaxial data: (a) deviatoric stress plotted against axial strain and (b) volumetric strain plotted against axial strain. Original data set retrieved from Abrantes & Yamamuro (2002)

friction and dilation angles, the model given here couples friction and dilation by way of using a stress–dilatancy equation. This gives a valuable and straightforward approach for capturing the non-linear behaviour of granular materials.

The yield surface is defined as the following, which is equivalent to the non-cohesive Mohr–Coulomb failure criterion

$$F(\boldsymbol{\sigma}, \eta_y) = q - \eta_y p' \tag{2}$$

where the state of plasticity is attained if $F(\boldsymbol{\sigma}, \eta_y) = 0$, with $\boldsymbol{\sigma}$ the stress tensor with invariants q and p', and η_y the mobilised stress ratio (Muir Wood, 2003). The mobilised stress ratio can be calculated using the stress–dilatancy relationship in equation (3), which is based on the seminal work of Nova & Muir Wood (1982).

$$\eta_y = M - D^{\mathrm{p}}(1 - N) \tag{3}$$

with M being the critical stress ratio for shearing at constant volume; N is Nova's volumetric coupling coefficient; and $D^{\mathrm{p}} = \mathrm{d}\varepsilon_{\mathrm{v}}^{\mathrm{p}}/\mathrm{d}\varepsilon_q^{\mathrm{p}}$ is the plastic dilatancy with $\mathrm{d}\varepsilon_{\mathrm{v}}^{\mathrm{p}}$ and $\mathrm{d}\varepsilon_q^{\mathrm{p}}$ the increment of plastic volumetric and deviatoric strain, respectively. In this work, equation (3) is directly connected to the deviatoric strain using a simple hardening/softening equation of the type (Andrade *et al.*, 2012)

$$D^{\mathrm{p}} = D_{\min}^{\mathrm{p}} h \varepsilon_q^{\mathrm{p}} \exp\left(1 - h\varepsilon_q^{\mathrm{p}}\right) \tag{4}$$

where $D_{\min}^{\mathrm{p}}$ is the minimum dilatancy and h is the hardening parameter.

Equations (2)–(4) set the basis for an inviscid elasto-plastic model that, up to this point, does not incorporate the effects of the loading rate. To overcome this limitation, the HSR effects on the model's state variable $\lambda^{\mathrm{vp}} = (\boldsymbol{n} \cdot \mathbf{D}^{\mathrm{vel}} \cdot \mathrm{d}\boldsymbol{\varepsilon} + \mathcal{L} \cdot \boldsymbol{b} \cdot \mathrm{d}\dot{\boldsymbol{\varepsilon}})/(\boldsymbol{n} \cdot \mathbf{D}^{\mathrm{vel}} \cdot \boldsymbol{m} + \mathcal{H})$ must be determined. First, the inertial coefficient I (da Cruz *et al.*, 2005) is introduced as a new state variable including the rate effects (i.e. $\boldsymbol{X}_{\mathrm{s}} = f(I)$). da Cruz *et al.* (2005) showed that the critical friction angle and dilation were connected to this parameter for rheology problems through a series of discrete simulations. Numerous studies have reproduced and validated these observations (Andrade *et al.*, 2012; Hurley & Andrade, 2015). The inertial coefficient is defined by

$$I = \mathcal{D}\dot{\varepsilon}_q \sqrt{\rho_{\mathrm{s}}/p'} \tag{5}$$

where $\mathcal{D}$ is the particle diameter; $\dot{\varepsilon}_q$ is the deviatoric strain rate, which replaces the shear strain rate ($\dot{\gamma}$) for stress path generalisation; and ρ_{s} the particle or solid density.

The inertial coefficient takes into account the effect of mobilising the weight of the particle at the enforced strain rate $\dot{\varepsilon}_q$ normalised by the confinement pressure p'. The evolution of the inertial coefficient plotted against the deviatoric strain is depicted in Fig. 3 for the YEA2011 data set, calculated with $\mathcal{D} = 0{\cdot}32$ mm and $\rho_{\mathrm{s}} = 2860$ kg/m^3.

Note that I decreases during the test as the axial strain increases, resulting from an increase in p', until it reaches a constant value during the last part of the test. Smooth changes in I are beneficial in ensuring the stability of the mathematical integration of the model. In the following subsection, the dependency of the model's elastic parameters and the state variable ($\eta_y(D^{\mathrm{p}})$) on I is established.

Evolution of the elastic and state variables with the strain rate

According to the studies of Abrantes & Yamamuro (2002) and Yamamuro *et al.* (2011), HSR increases the Young's modulus up to 115%. Consistently, the implementation of a non-stationary yield surface requires expressions relating the state variables and the strain rate. These expressions work as strain-rate hardening/softening laws and they can be phenomenological or analytical.

Figure 4 presents the stress–dilatancy plots for the YEA2011 data set grouped by confinement stress and initial void ratio (Figs 4(a)–4(d)). The purpose of these graphs is to provide an overview of the phenomena associated with strain rate and inertial effects. Generally, the stress ratio increases in lockstep with the strain rate in all subplots. Moreover, the paths show a vertical line that shifts to the left, indicating less contraction. In contrast, enhanced dilation is visible only in Fig. 4(b), whereas apparent reduced dilation is observed in the remaining tests in Figs 4(a), 4(c) and 4(d). This is attributed to shear banding preventing samples from reaching minimum dilatancy (e.g. tests with $e_0 = 1{\cdot}03$ in Figs 4(a) and 4(c)), or severe dilation reversal due to oscillations in the volumetric strain response (e.g. tests with

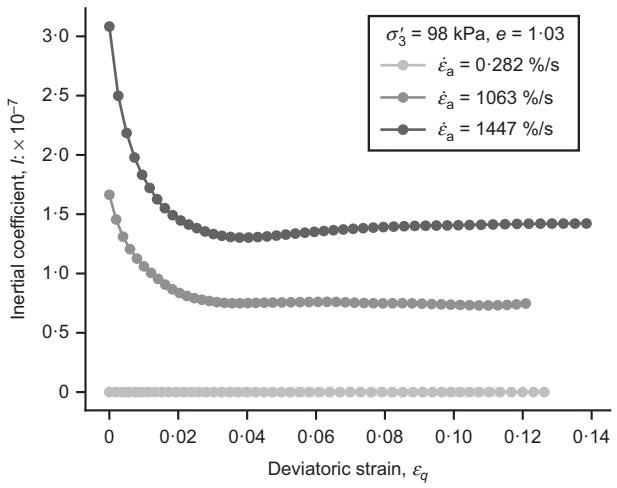

Fig. 3. Evolution of the inertial coefficient plotted against the deviatoric strain for the soil sample with σ_3' = 98 kPa and e = 1·03. Similar results are obtained for all triaxial tests

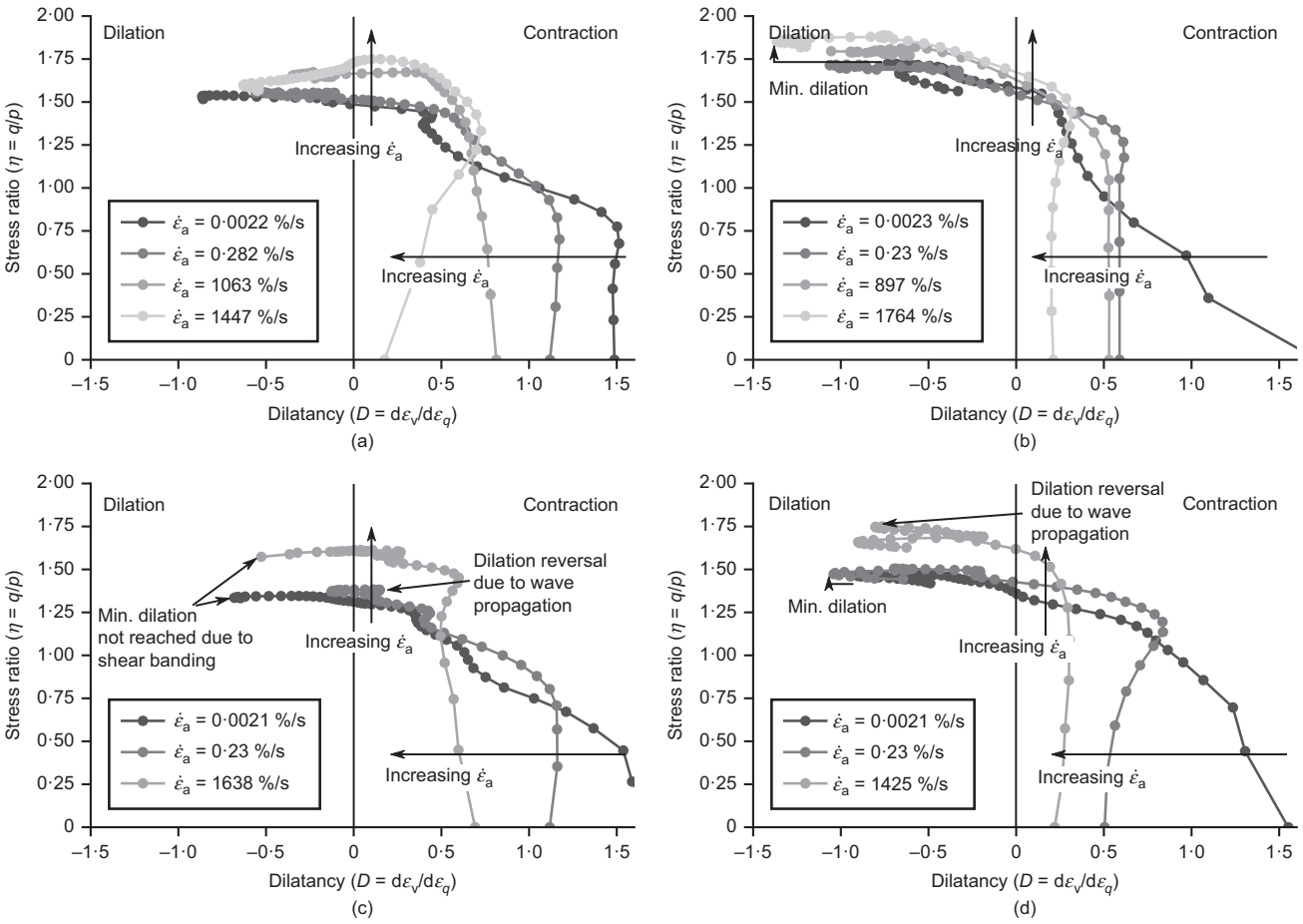

Fig. 4. Dilatancy plots under HSR. The plots are arranged according to initial confinement pressure σ_3' and initial void ratio e_0: (a) σ_3' = 98 kPa; e = 1·03; (b) σ_3' = 98 kPa; e = 0·93; (c) σ_3' = 350 kPa; e = 1·03; (d) σ_3' = 350 kPa; e = 0·93

$\dot{\varepsilon}_a = 1425\%/s$ in Fig. 4(d)). Therefore, the minimum dilation for tests in Figs 4(a), 4(c) and 4(d) is not fully reliable. Nonetheless, it is clear that HSR affects stress–dilatancy. As a result, the strain-rate hardening/softening equations can be derived using a work–energy dissipation procedure.

Consider the rate of elastic strain work ($\dot{W}$) in a viscoplastic material using equation (6) (see Appendix 1)

$$\dot{W} = p\dot{\varepsilon}_v + q\dot{\varepsilon}_q + p^v\dot{\varepsilon}_v + q^v\dot{\varepsilon}_q \tag{6}$$

with superscript $(\cdot)^v$ reserved for viscous quantities. By the superposition principle, equation (6) can be particularised for viscoelastic components and reworked to the form shown in equation (7) (see Appendix 1)

$$M^{vel} = G/K + \eta^{el} + f(I) \tag{7}$$

with M^{vel} the elastic energy–work dissipation density. According to equation (7), the G/K ratio ($\partial\varepsilon_v^{el}/\partial\varepsilon_q^{el} = G/K$) is independent of the stress ratio, which is consistent with the vertical lines observed at the beginning of the stress–dilation paths corresponding to elastic behaviour (Fig. 4). Increased strain rate results in increased G/K ratio (vertical lines move toward the left in Fig. 4) and prolonged elastic behaviour (vertical lines are higher). Assuming that the initial soil fabric and properties are identical, this is only possible if the yield surface expands as the strain rate increases, which indicates a non-stationary yield surface.

From equation (7), the change in the G/K ratio is expressed as

$$\Delta(G/K)/(G/K) \propto \Delta I f'(I)/f(I) \tag{8}$$

where the function $f(I)$ connects G/K and I (see Appendix 1). Integrating equation (8) with limits $G/K = G_0/K_0 \rightarrow I = I_0$, with $I_0 =$ reference inertial coefficient, results in a power function that relates the dilation and inertial coefficient ratios as described by equations (9) and (10), which satisfy equation (8).

$$G/G_0 = (I/I_0)^{\kappa_G} \approx (\dot{\varepsilon}_q/\dot{\varepsilon}_{ref})^{\kappa_G} \tag{9}$$

$$K/K_0 = (I/I_0)^{\kappa_K} \approx (\dot{\varepsilon}_q/\dot{\varepsilon}_{ref})^{\kappa_K} \tag{10}$$

with $\kappa_K > \kappa_G$ to produce reduction of G/K with increasing strain rate. If $\kappa_K = \kappa_G$ the model will produce rate-independent Poisson's ratio and does not capture the elastic contraction behaviour depicted in Fig. 4. Note that the inertial coefficient ratio is equivalent to the strain rate ratio ($\dot{\varepsilon}_q/\dot{\varepsilon}_{ref}$) with $\dot{\varepsilon}_{ref}$ = the reference strain rate.

The Young's modulus is obtained from the YEA2011 data set. In particular, the Young's modulus values are calculated as the secant modulus at 1% axial strain and converted to shear and bulk modulus using $G = E/2(1 + v)$ and $K = E/3(1 - 2v)$, where Poisson's ratio (v) is assumed to be equal to 0·2. It is important to note that a back-calculation of Poisson's ratio using Muir Wood (2003) and Duncan & Chang (1970) yields disparate negative values, probably related to how the strains were measured by Abrantes & Yamamuro (2002). Only for the test with $\sigma_3' =$ 98 kPa and $e_0 = 0{\cdot}94$ is the Poisson's ratio equal to 0·2, and hence the assumed value. Elastic parameters for quasi-static strain rates serve as a baseline for comparison with those with HSR.

Figure 5(a) shows the evolution of the shear modulus with the inertial coefficient. It is seen that the YEA2011 data points fit the proposed model well with $\kappa_G = 0{\cdot}06$. Uncertainty for high I/I_0 ratios is attributed to pressure dependency not being considered and wave oscillations in the YEA2011 data set (as already discussed in the previous section) that could slightly alter the calculation of the secant modulus. In addition, the influence of the inertial coefficient on the G/K ratio is depicted in Fig. 5(b). It is observed that there is a significant scatter, probably due to assuming that all samples have the same Poisson's ratio.

Utilising various Poisson's ratios for each test and adding pressure-dependent elasticity adds additional complexity to the constitutive model. Henceforth, a simple relation between κ_K and κ_G is proposed. In Fig. 5(b) it can be observed that $\kappa_K = 2\kappa_G$ yields acceptable results for a subset of points comprising primarily tests with loose sand. However, $\kappa_K = 3\kappa_G$ is more appropriate for dense configuration tests. The relation $\kappa_K = 2{\cdot}5\kappa_G$ is proposed since it returns an average value of the dilatancy ratio and henceforth is used in further simulations.

Following the same strategy as for the elastic parameters, equation (11) is derived from the dissipation of plastic work (see Appendix 1).

$$M^{\mathrm{vp}} = D^{\mathrm{p}} + \eta_y + f(I) \tag{11}$$

with M^{vp} the viscoplastic energy dissipation rate.

The behaviour observed in Fig. 4 appears to be consistent with equation (11). It is seen that as the strain rate increases, the observed stress ratio increases as all paths move upward. When the critical state is attained $D^{\mathrm{p}} = 0$, then equation (11) is transformed into

$$M^{\mathrm{vp}} = \eta_{y,\mathrm{c}} + f(I_{\mathrm{c}}) \tag{12}$$

with the critical condition denoted by the subscript $(\cdot)_{\mathrm{c}}$. It is deduced from equation (12) that the critical stress ratio is masked by inertial effects, as numerous authors have demonstrated (da Cruz *et al.*, 2005; Jop *et al.*, 2006; Andrade *et al.*, 2012; Hurley & Andrade, 2015). Under relatively large confinement stress, in contrast, inertial effects become less important (as $p \uparrow$, $I < 0{\cdot}001$ in equation (5)) and the critical stress ratio remains theoretically unchanged. The latest is the case with the YEA2011 data set, as previously reported by Zambrano-Cruzatty (2021).

Additional evidence for a rate-independent critical stress ratio is presented in Fig. 6(a), which contains the maximum stress ratio ($\eta_{\max}$) plotted against the minimum dilatancy ($D_{\min}$) for all experiments. The colour coding in Fig. 6(a) denotes different strain-rate levels, the white crosses indicate the confinement pressure, and the dashed line with arrows separates data points with different initial void ratios. As depicted in Fig. 6(a), a linear fitting model with $M_{\mathrm{tc}} = 1{\cdot}4$ can be constructed for most points (line 1 in Fig. 6(a)), implying that the critical stress ratio is strain-rate independent. This is consistent with the widely accepted assumption that M_{tc} is commensurate with the mineral-to-mineral

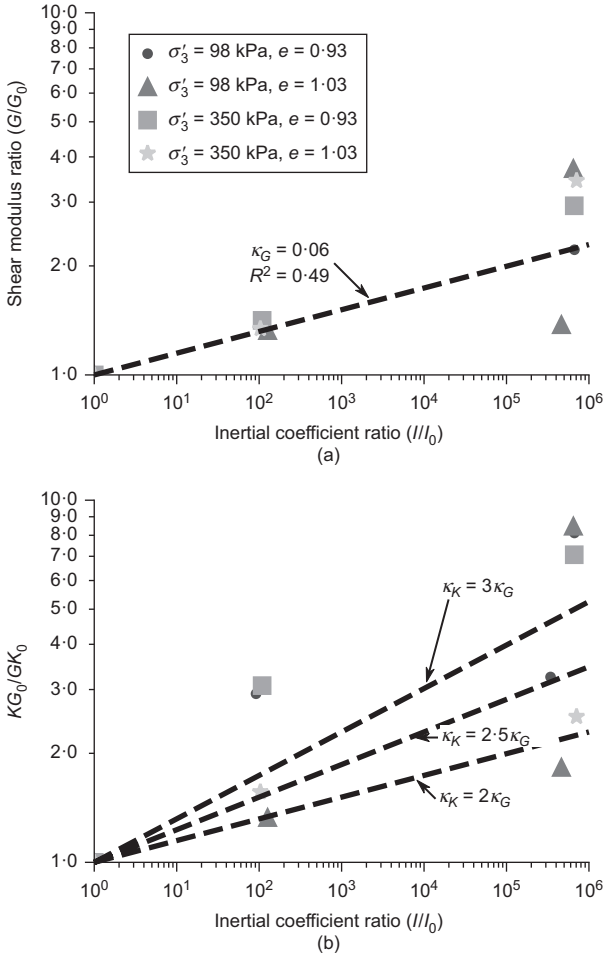

Fig. 5. Rate effects on the elastic parameters: (a) shear modulus ratio plotted against inertial coefficient; (b) G/K ratio plotted against inertial coefficient ratio

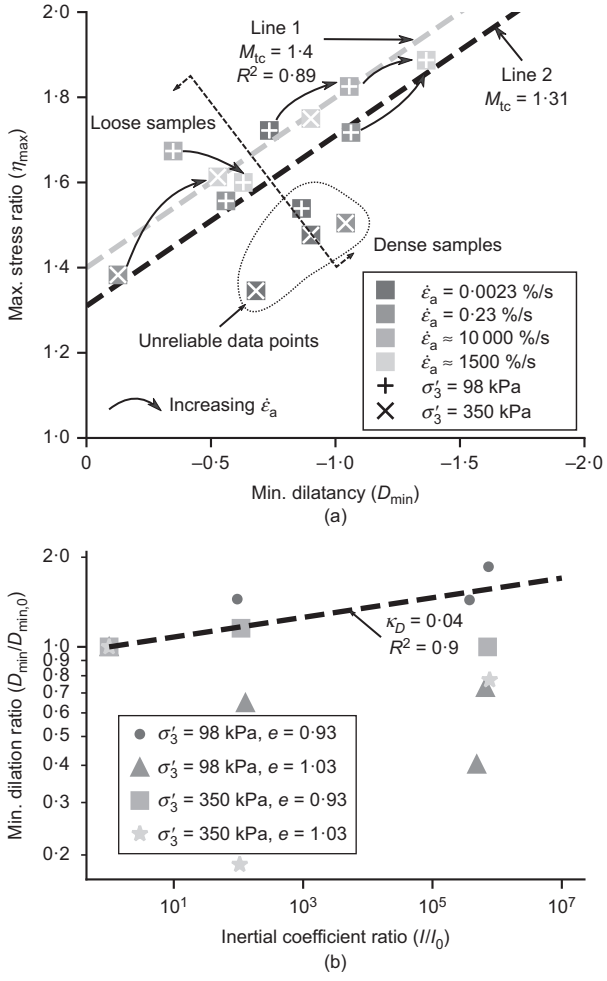

Fig. 6. Rate and inertial effects on the critical stress ratio and the minimum dilation: (a) maximum stress ratio ($\eta_{\max}$) plotted against minimum dilatancy ($D_{\min}$) with annotated effect of the strain rates on the dilatancy; (b) dilatancy ratio ($D_{\min}/D_{\min,0}$) plotted against the inertial coefficient ratio (I/I_0)

friction coefficient. A smaller group of tests, mainly corresponding to $\sigma'_3 = 350$ kPa, are slightly off trend. Overall, an average $M_{tc} = 1{\cdot}31$ is obtained when all points are considered, which is in good agreement with the critical stress ratio used in Higgins *et al.* (2013) and Xu & Zhang (2015) for the YEA2011 data set. The outlier points correspond to tests that suffer from artefacts attributed to shear banding that prevent samples from reaching minimum dilatancy or severe dilation reversal due to oscillations in the volumetric strain response, as discussed previously in this section. Therefore, the dilation measurements of these four points have been reasonably considered unreliable.

Theoretical (equation (11)) and experimental evidence (e.g. Fig. 1) indicate that strain-rate hardening must occur as a result of changes in the plastic dilation. This is observed in Fig. 6(a) where the majority of points with the same initial void ratio and confinement pressure shift to the right (i.e. $|D_{min}|$ increases) as the strain rate increases. This indicates that a higher stress ratio is achieved precisely as a result of the enhanced dilation.

By analogy with the G/K ratio, equation (8) serves to model the changes in minimum plastic dilation under HSR.

$$D^p_{min}/D^p_{min,0} = (I/I_0)^{\kappa_D} \tag{13}$$

with $D^p_{min,0}$ being the inviscid minimum plastic dilation and κ_D the 'dilation viscosity' coefficient. Fig. 6(b) shows a plot of dilation ratio ($D_{min}/D_{min,0}$) against the inertial coefficient ratio (I/I_0) to validate equation (13). The points for the tests at which minimum dilation is achieved (Fig. 4(b)) are observed to follow a growing trend (i.e. $D_{min}/D_{min,0} > 1$) as indicated by the regression line with $\kappa_D = 0{\cdot}04$. Consistently, the dilation ratio for the remaining data sets has significant scatter, since the comparison with the quasi-static dilation is not reliable (i.e. $D_{min}/D_{min,0} < 1$). Moreover, results from other studies (Omidvar *et al.*, 2012; Suescun-Florez & Iskander, 2017) show that the increase in the maximum deviatoric strain, and therefore the dilation, is highly correlated with the initial confinement pressure and void ratio, which are not directly considered in equation (13). In the subsequent section, equation (13) will be revisited to show that its formulation is consistent with Perzyna's viscoplasticity to add a supporting proof for its suitability.

Finally, Table 1 summarises the model's equations and Table 2 (presented in the calibration section below) summarises the value of the parameters determined from the YEA2011 data set.

A CONSISTENCY APPROACH TO VISCOPLASTICITY

Stress, strain and strain-rate relationship

In this study, viscous effects are incorporated by updating the internal state variables due to changes in the strain-rate tensor ($\dot{\boldsymbol{\varepsilon}}$), which is defined as the time derivative of the strain tensor $\dot{\boldsymbol{\varepsilon}} = \mathrm{d}\boldsymbol{\varepsilon}/\mathrm{d}t$. It is convenient to assume that the stress–strain ($\boldsymbol{\sigma}$ plotted against $\boldsymbol{\varepsilon}$) of soils follows an isotach behaviour. This means that the stress–strain response at different steady strain rates is unique (Fig. 7(a)). A stress path can move from one strain rate and inertial level, say at $\dot{\boldsymbol{\varepsilon}}_0$ and I_0, to another strain rate $\dot{\boldsymbol{\varepsilon}}_f$ and I_f, as illustrated by the arrow in Fig. 7(a). Extrapolating to three dimensions, the increase in viscoplastic stress ($\mathrm{d}\boldsymbol{\sigma}^{vp}$) produced by this path is expressed by equation (14).

$$\mathrm{d}\boldsymbol{\sigma}^{vp} = \mathbf{D}^{vel} \cdot \mathrm{d}\boldsymbol{\varepsilon}^{vel} = \mathbf{D}^{vel} \cdot (\mathrm{d}\boldsymbol{\varepsilon} - \mathrm{d}\boldsymbol{\varepsilon}^{vp}) \tag{14}$$

where $\mathbf{D}^{vel}$ is the viscoelastic constitutive matrix; $\mathrm{d}\boldsymbol{\varepsilon}^{vel}$ is the viscoelastic portion of the strain increment; $\mathrm{d}\boldsymbol{\varepsilon}^{vp}$ is the viscoplastic strain increment, and $\mathrm{d}\boldsymbol{\varepsilon}$ is the total strain increment.

The relationship between strain and strain rate is also required, particularly when substepping is needed for numerical integration. Fig. 7(b) shows an idealised relationship between the strain and the strain rate for a one-dimensional response. A linear relationship can be assumed with sufficient accuracy providing a small strain substepping approach as it is expressed in equation (15).

$$\mathrm{d}\dot{\boldsymbol{\varepsilon}} = c\,\mathrm{d}\boldsymbol{\varepsilon} \tag{15}$$

where c is a constant scalar. In three-dimensional space, equation (15) implies that the increments of strain rate and strain are parallel, which can be assumed with reasonable accuracy if the increment of strain is sufficiently small.

Consistency equation, viscoplastic strain and viscoplastic stress

Consider a material model with a yield function $F(\boldsymbol{\sigma}, \boldsymbol{X}_s)$ depending on the stress tensor ($\boldsymbol{\sigma}$) and a set of internal state variables $\boldsymbol{X}_s = \{X_{s,1}, X_{s,2}, X_{s,3}, \ldots, X_{s,n}\}$, in which the internal state variables can harden/soften as a function of the plastic strain and the strain rate such that $X_{s,i} = f_i(\boldsymbol{\varepsilon}^{vp}, \dot{\boldsymbol{\varepsilon}})$. The consistency equation enforces that any set of stress and state variables remain on the yield surface once plasticity is attained (i.e. $\mathrm{d}F = 0$).

Table 1. Summary of model equations and internal state variables

Model component	Equations
Model's internal state variables ($\boldsymbol{X}_s$)	η_y, D^p and I with $\eta_y = M - D^p(1 - N)$ $I = \mathcal{D}\dot{\varepsilon}_q\sqrt{\rho_s/p'}$
Yield surface	$F = q - p'\eta_y$
Plastic potential	$P = q + p'D^p$
Hardening rule	$D^p = D^p_{min} h\varepsilon^p_q \exp(1 - h\varepsilon^p_q)$
Strain-rate hardening rule	$D^p_{min}/D^p_{min_0} = (I/I_0)^{\kappa_D}$
Elasticity	$G/G_0 = (I/I_0)^{\kappa_G}$ $K/K_0 = (I/I_0)^{\kappa_K}$

Table 2. Summary of elastic and state variables. The bulk modulus is obtained assuming $\nu = 0{\cdot}2$

$e - \sigma'_3$: kPa	G_0: MPa	M_{tc}	D_{min}	N	h
0·98–98	6·1	1·31	−0·58	0·30	20
1·03–98	3·9	1·31	−0·32	0·30	18
0·98–350	18·6	1·31	−0·24	0·30	17
1·03–350	12·4	1·31	−0·1	0·30	8

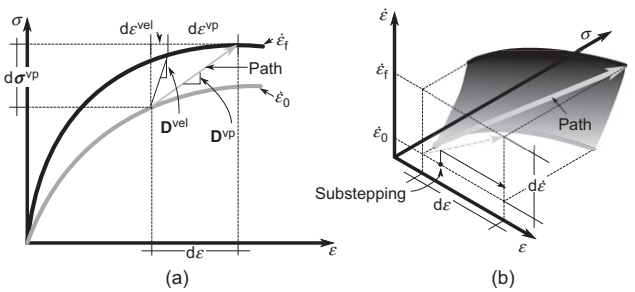

Fig. 7. Schematic stress–strain response of materials: (a) one-dimensional isotach stress–strain response of soils; (b) three-dimensional visualisation of a transient strain-rate path and its relationship with substepping schemes

The viscoplastic increment of strain ($\mathrm{d}\boldsymbol{\varepsilon}^{\mathrm{vp}}$) is computed by the flow rule, which in the case of the non-associated flow rule is expressed by equation (16).

$$\mathrm{d}\boldsymbol{\varepsilon}^{\mathrm{vp}} = \lambda^{\mathrm{vp}}\boldsymbol{m} \tag{16}$$

where λ^{vp} is the so-called plastic multiplier and $\boldsymbol{m} = \partial P/\partial\boldsymbol{\sigma}$ is the vector normal to the plastic potential function P; defined in terms of the stress and internal state variables ($P = f(\sigma, \boldsymbol{X}_{\mathrm{s}})$). Recall that Perzyna's viscoplasticity uses equation (1) explicitly to find the plastic strain tensor. If $P = q + D^{\mathrm{p}}p'$ is the plastic potential function, $\partial P/\partial p = D^{\mathrm{p}}$. For the consistency–viscoplasticity $\partial P/\partial p = D_0^{\mathrm{p}}(I/I_0)^{\kappa_D}$ and henceforth $\mathrm{d}\dot{\boldsymbol{\varepsilon}} \propto D_0^{\mathrm{p}}(I/I_0)^{\kappa_D}$. This shows that, for the proposed model, the consistency–viscoplasticity is equivalent to Perzyna's with $\Phi = (I/I_0)^{\kappa_D}$. Similar parallelism has been demonstrated by other researchers (Wang *et al*., 1997; Heeres *et al*., 2002; Liingaard *et al*., 2004).

Combining equations (15) and (16) with the consistency condition ($\mathrm{d}F = 0$), the consistency equation considering strain-rate effects is obtained as (see Appendix 1)

$$\boldsymbol{n}\cdot\mathbf{D}^{\mathrm{vel}}\cdot\mathrm{d}\boldsymbol{\varepsilon} - \lambda^{\mathrm{vp}}\boldsymbol{n}\cdot\mathbf{D}^{\mathrm{vel}}\cdot\boldsymbol{m} + \lambda^{\mathrm{vp}}\boldsymbol{L}\cdot\boldsymbol{a}\cdot\boldsymbol{m} + \boldsymbol{L}\cdot\boldsymbol{b}\cdot\mathrm{d}\dot{\boldsymbol{\varepsilon}} = 0 \tag{17}$$

where $\boldsymbol{n} = \partial F/\partial\boldsymbol{\sigma}$ is a vector normal to the yield surface, $\boldsymbol{L} = \partial F/\partial\boldsymbol{X}_{\mathrm{s}}$ is the direction of maximum change of the yield function with respect to the internal state variables, $\boldsymbol{a} = \partial\boldsymbol{X}_{\mathrm{s}}/\partial\boldsymbol{\varepsilon}^{\mathrm{vp}}$ is the derivative of the internal state variables with respect to the plastic strain, and $\boldsymbol{b} = \partial\boldsymbol{X}_{\mathrm{s}}/\partial\dot{\boldsymbol{\varepsilon}}$ is the derivative of the internal state variables with respect to the strain rate.

At this point, two integration strategies are considered. The first takes into account the original assumption of Wang *et al*. (1997), in which the elastic portion of the increment of strain ($\mathrm{d}\boldsymbol{\varepsilon}^{\mathrm{ve}}$) is insensitive to the strain rate ($\mathrm{d}\dot{\boldsymbol{\varepsilon}}^{\mathrm{vel}} = 0$), hence the increment of strain rate can be expressed using equation (18).

$$\mathrm{d}\dot{\boldsymbol{\varepsilon}} \approx \lambda^{\mathrm{vp}}\boldsymbol{m}/\Delta t \tag{18}$$

Note that Wang *et al*. (1997) proposed this approach specifically for the von Mises model, which contrasts with the generalised mathematical implementation presented herein. In this work, this approach is called the 'original' consistency viscoplasticy. Alternatively, a variation of this method is proposed, where the increment of strain rate ($\mathrm{d}\dot{\boldsymbol{\varepsilon}}$) is used without further decomposition between plastic and elastic portions. For which reason, no assumptions are needed regarding the elastic strain rate. This variation is termed the 'dashpot method'. The treatment of the strain rate as an internal parameter is a special case of the non-stationary yield surface theory proposed by Olszak & Perzyna (1966).

The original consistency variant. The increment of viscoplastic stress is found by substituting equation (18) in equation (17) and subsequently solving for the plastic multiplier (λ^{vp}). Equation (19) shows the result of this operation

$$\lambda^{\mathrm{vp}} = \frac{\boldsymbol{n}\cdot\mathbf{D}^{\mathrm{vel}}\cdot\mathrm{d}\boldsymbol{\varepsilon}}{\boldsymbol{n}\cdot\mathbf{D}^{\mathrm{vel}}\cdot\boldsymbol{m} + \mathcal{H}^{\mathrm{vp}}} \tag{19}$$

where the viscoplastic hardening/softening term ($\mathcal{H}^{\mathrm{vp}}$) is given by equation (20).

$$\mathcal{H}^{\mathrm{vp}} = \mathcal{H} - \boldsymbol{L}\cdot\boldsymbol{b}\cdot\boldsymbol{m}/\Delta t \tag{20}$$

where $\mathcal{H}$ is a hardening/softening term expressed by

$$\mathcal{H} = -\boldsymbol{L}\cdot\boldsymbol{a}\cdot\boldsymbol{m} \tag{21}$$

Finally, equations (19), (16) and (14) are combined to obtain equation (22)

$$\mathrm{d}\boldsymbol{\sigma}^{\mathrm{vp}} = \mathbf{D}^{\mathrm{vel}}\cdot\mathrm{d}\boldsymbol{\varepsilon} - \mathbf{D}^{\mathrm{vel}}\cdot\boldsymbol{m}\left(\frac{\boldsymbol{n}\cdot\mathbf{D}^{\mathrm{vel}}\cdot\mathrm{d}\boldsymbol{\varepsilon}}{\boldsymbol{n}\cdot\mathbf{D}^{\mathrm{vel}}\cdot\boldsymbol{m} + \mathcal{H}^{\mathrm{vp}}}\right) \tag{22}$$

which can be simplified as shown in equation (23).

$$\mathrm{d}\boldsymbol{\sigma}^{\mathrm{vp}} = \mathbf{D}^{\mathrm{vp}}\cdot\mathrm{d}\boldsymbol{\varepsilon} \tag{23}$$

where $\mathbf{D}^{\mathrm{vp}}$ is the viscoplastic constitutive matrix which is given by equation (24).

$$\mathbf{D}^{\mathrm{vp}} = \mathbf{D}^{\mathrm{vel}} - \frac{\mathbf{D}^{\mathrm{vel}}\cdot\boldsymbol{m}\otimes\boldsymbol{n}^{\mathrm{T}}\cdot\mathbf{D}^{\mathrm{vel}}}{\boldsymbol{n}\cdot\mathbf{D}^{\mathrm{vel}}\cdot\boldsymbol{m} + \mathcal{H}^{\mathrm{vp}}} \tag{24}$$

In which $\otimes$ represents the tensor product operator.

The dashpot method variant. Equation (25) is retrieved by solving for λ^{vp} in equation (17).

$$\lambda^{\mathrm{vp}} = \frac{\boldsymbol{n}\cdot\mathbf{D}^{\mathrm{vel}}\cdot\mathrm{d}\boldsymbol{\varepsilon} + \boldsymbol{L}\cdot\boldsymbol{b}\cdot\mathrm{d}\dot{\boldsymbol{\varepsilon}}}{\boldsymbol{n}\cdot\mathbf{D}^{\mathrm{vel}}\cdot\boldsymbol{m} + \mathcal{H}} \tag{25}$$

Replacing equation (25) in equation (16) and then in equation (14), one can obtain the increment of viscoplastic stress.

$$\mathrm{d}\boldsymbol{\sigma}^{\mathrm{vp}} = \mathbf{D}^{\mathrm{vel}}\cdot\mathrm{d}\boldsymbol{\varepsilon} - \mathbf{D}^{\mathrm{vel}}\cdot\boldsymbol{m}\left(\frac{\boldsymbol{n}\cdot\mathbf{D}^{\mathrm{vel}}\cdot\mathrm{d}\boldsymbol{\varepsilon} + \boldsymbol{L}\cdot\boldsymbol{b}\cdot\mathrm{d}\dot{\boldsymbol{\varepsilon}}}{\boldsymbol{n}\cdot\mathbf{D}^{\mathrm{vel}}\cdot\boldsymbol{m} + \mathcal{H}}\right) \tag{26}$$

Equation (26) can be rearranged and simplified as shown below

$$\mathrm{d}\boldsymbol{\sigma}^{\mathrm{vp}} = \mathbf{D}^{\mathrm{ep}}\cdot\mathrm{d}\boldsymbol{\varepsilon} + \mathbf{C}^{\mathrm{vp}}\cdot\mathrm{d}\dot{\boldsymbol{\varepsilon}} \tag{27}$$

where $\mathbf{D}^{\mathrm{ep}}$ is the inviscid elastoplastic constitutive matrix, and $\mathbf{C}^{\mathrm{vp}}$ is a viscoplastic damping matrix described by equation (28)

$$\mathbf{C}^{\mathrm{vp}} = -\frac{\mathbf{D}^{\mathrm{vel}}\cdot\boldsymbol{m}\otimes(\boldsymbol{L}\cdot\boldsymbol{b})^{\mathrm{T}}}{\boldsymbol{n}\cdot\mathbf{D}^{\mathrm{vel}}\cdot\boldsymbol{m} + \mathcal{H}} \tag{28}$$

Equation (27) resembles a three-dimensional Kelvin model, in which a dashpot and a spring are connected in parallel. Hence, the name of this variant of the consistency approach.

NUMERICAL IMPLEMENTATION

The numerical implementation follows the refined explicit integration scheme (REIS) proposed by Sloan *et al*. (2001). This was developed for inviscid elastoplasticity. The REIS implementation is chosen because it provides a robust framework that is more stable for consistency approaches; however, the consistency method could also be used with other integration schemes. This section describes the numerical integration of constitutive equations. Detailed pseudo-algorithms are presented in Appendix 2.

Main algorithm

In the following, the symbol $\Delta(\cdot)$ represents the change of a variable between two consecutive steps ($(\cdot)_{i+1} - (\cdot)_i$), the subscript $(\cdot)_0$ represents initial or inviscid values and the subscript $(\cdot)_{\mathrm{u}}$ denotes the updated state.

The calculation starts with the initialisation of parameters including the initial stress tensor ($\boldsymbol{\sigma}_0$), state variables ($\boldsymbol{X}_{\mathrm{s},0}$), strain-rate tensor ($\dot{\boldsymbol{\varepsilon}}_0$), increment of strain ($\Delta\varepsilon$), time

increment (Δt) and elastic properties included in the elasticity matrix ($\mathbf{D}_0^{\text{vel}}$). Once the model variables are initialised, the current strain rate and strain-rate invariants can be computed.

As mentioned in the previous section, strain-rate hardening/softening controls the yield function size dynamically; thus, negative strain rate increments might cause over-softening of internal state variables. As a result, it is convenient to establish a strain-rate threshold under which the material behaviour is considered to be quasi-static and no additional softening is permitted. Fig. 8(a) depicts the three strain-rate paths for which the internal state variables need to be updated. Paths 1 and 3 cross the threshold and path 2 indicates strain-rate change. Contrarily, Fig. 8(b) shows examples of paths where the internal state variables do not need updating. The algorithm 1 is designed to evaluate the condition above using the deviatoric strain-rate invariant ($\dot{\varepsilon}_q$) and can be found in Appendix 2.

Subsequently, the elastic-predictor stress ($\boldsymbol{\sigma}^{\text{vel}}$) can be calculated with the updated state and elastic parameters (i.e. $\mathbf{D}_{\text{u}}^{\text{vel}}$ and $\boldsymbol{X}_{\text{s,u}}$), and then the yield function can be evaluated on the updated stress ($F(\boldsymbol{\sigma}_0 + \Delta\boldsymbol{\sigma}^{\text{vel}}, \boldsymbol{X}_{\text{s,u}})$) to determine if plasticity is attained within the bounds of a numerical tolerance for the yield function ($F(\boldsymbol{\sigma}_0 + \Delta\boldsymbol{\sigma}^{\text{vel}}, \boldsymbol{X}_{\text{s,u}}) > \text{FTOL}$, where FTOL denotes yield function tolerance).

After this, the yield function is evaluated on the initial stress ($F(\boldsymbol{\sigma}_0, \boldsymbol{X}_{\text{s,0}})$) to determine the proportion of elastic to plastic strains (α). Three scenarios are possible: (a) the stress state undergoes an elastoplastic transition ($0 < \alpha < 1$); (b) the stress state experiences pure plasticity ($\alpha = 0$); or (c) the stress state transitions from plasticity to elasticity, and then goes back to plasticity. These states can be assessed using the value of the yield function in the initial state and elastic parameters and using either the Pegasus algorithm described in Sloan *et al.* (2001) or the Newton–Raphson method used here.

To check for unloading in plasticity, the angle between the normal to the yield surface ($\boldsymbol{n}$) and the elastic predictor increment of stress are evaluated ($\Delta\boldsymbol{\sigma}^{\text{vel}}$) as is show in equation (29).

$$\beta_F = \arccos\left(\frac{\boldsymbol{n} \cdot \Delta\boldsymbol{\sigma}^{\text{vel}}}{||\boldsymbol{n}||_2 ||\Delta\boldsymbol{\sigma}^{\text{vel}}|_2}\right) \tag{29}$$

where $||\cdot||_2$ is the L-two norm of the tensors. If β_F is larger than 90° the material experiences elastoplastic unloading, which will require the determination of the elastic unloading proportion ($\alpha\Delta\varepsilon$). More detail is presented in the main REIS algorithm (algorithm 2 in Appendix 2).

Elastoplastic transition calculation

Calculation of the elastic proportion ($\alpha\Delta\boldsymbol{\varepsilon}^{\text{vel}}$) is needed when there is elastoplastic loading or elastoplastic unloading (algorithm 2) from an elastic state. An example of the former is illustrated in Fig. 9. When the stress is inside the elastic area, the yield surface (F) can shrink or expand dynamically because of the strain-rate softening/hardening processes. A situation that may arise is that the strain rate softens the yield surface while the stress increases. For instance, in Fig. 9(a), the initial yield surface (black dashed line) is dragged to its final position (grey dashed line). The stress path will satisfy $F_{\text{T}} = F(\boldsymbol{\sigma}_0 + \Delta\boldsymbol{\sigma}^{\text{vel}}, \boldsymbol{X}_{\text{s,u}}) > \text{FTOL}$ and $F_0 = F(\boldsymbol{\sigma}_0, \boldsymbol{X}_{\text{s,0}}) < \text{FTOL}$

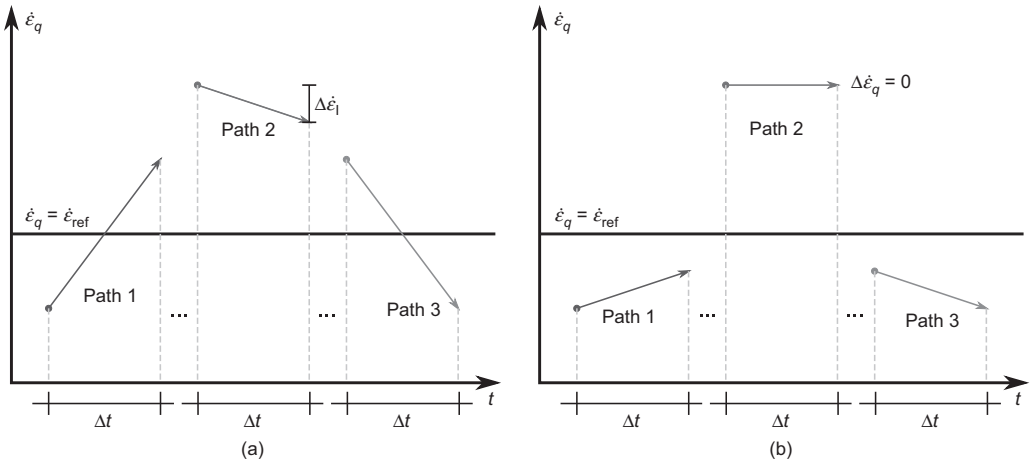

Fig. 8. Schematic representation of strain-rate paths: (a) shows the possible paths that will harden/soften the state variables; (b) shows examples of paths where the state variables will not be updated

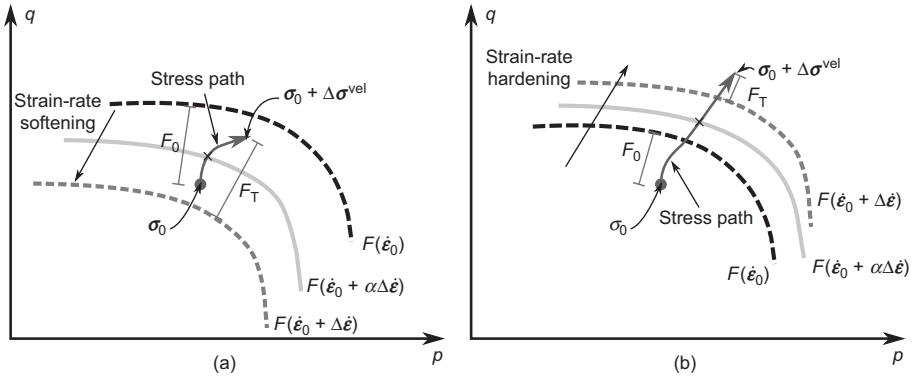

Fig. 9. (a) A stress path under elastoplastic loading with a shrinking yield surface and (b) with an expanding yield surface

. Hence, there is a point at which the stress path and the shrinking yield surface intersect, as is illustrated by the continuous grey yield surface. Similarly, this situation also arises if the yield surface expands at a slower pace than the stress rate (Fig. 9(b)). To calculate the proportion α at which this event occurs, a Newton–Raphson method is used.

Assume a positive α such that the strain and strain rates can be decomposed into their plastic and elastic proportions (equations (30) and (31)).

$$\Delta\boldsymbol{\varepsilon}^{\text{vel}} = \alpha\Delta\boldsymbol{\varepsilon} \tag{30}$$

$$\Delta\dot{\boldsymbol{\varepsilon}}^{\text{vel}} = \alpha\Delta\dot{\boldsymbol{\varepsilon}} \tag{31}$$

Equation (31) is applicable if the strain and strain rates are linearly related as was established in equation (15).

If the strain-rate hardening/softening equations are bijective, there is a unique set of internal state variables that correspond to a certain level of strain rate, such that one can determine those variables using $\boldsymbol{X}_{\text{s},\alpha} = \boldsymbol{f}\left(\boldsymbol{X}_{\text{s},0}, \dot{\varepsilon}_{q,0} + \alpha\Delta\dot{\boldsymbol{\varepsilon}}\right)$, where $\boldsymbol{f}$ represents the set of hardening/softening equations (e.g. equation (13)). Similarly, there exists a stress state $\boldsymbol{\sigma}_\alpha = \boldsymbol{\sigma}_0 + \Delta\boldsymbol{\sigma}_\alpha^{\text{vel}}$ that satisfies $F\left(\boldsymbol{\sigma}_\alpha, \boldsymbol{X}_{\text{s},\alpha}\right) = 0$, where $\Delta\boldsymbol{\sigma}_\alpha^{\text{vel}} = \alpha\mathbf{D}_\alpha^{\text{vel}} \cdot \Delta\dot{\boldsymbol{\varepsilon}}$, and $\mathbf{D}_\alpha^{\text{vel}}$ is the updated viscoelastic constitutive matrix at $\Delta\boldsymbol{\varepsilon}^{\text{vel}}$ and $\Delta\dot{\boldsymbol{\varepsilon}}^{\text{vel}}$. Hence, it is possible to find α by iterating equation (32)

$$\alpha^{i+1} = \alpha^i - F\left(\alpha^i\right)/F'_\alpha\left(\alpha^i\right) \tag{32}$$

where $F(\alpha^i)$ is the yield function evaluated at α^i, and $F'_\alpha(\alpha^i)$ is the partial derivative of F with respect to α evaluated at α^i, and i represents the iteration step.

The derivative of the yield function with respect to α can be computed using equation (33)

$$F'_\alpha = \boldsymbol{n} \cdot \left[\mathbf{D}_\alpha^{\text{vel}} \cdot \Delta\boldsymbol{\varepsilon} + \alpha\Delta\boldsymbol{\varepsilon} \cdot \left(\partial\mathbf{D}^{\text{vel}}/\partial\dot{\boldsymbol{\varepsilon}}\right) \cdot \Delta\dot{\boldsymbol{\varepsilon}}\right] + \boldsymbol{L} \cdot \boldsymbol{b} \cdot \Delta\dot{\boldsymbol{\varepsilon}} \tag{33}$$

Note that the terms $\left(\partial\mathbf{D}^{\text{vel}}/\partial\dot{\boldsymbol{\varepsilon}}\right) \cdot \Delta\dot{\boldsymbol{\varepsilon}}$ and $\left(\partial\boldsymbol{X}_{\text{s}}/\partial\dot{\boldsymbol{\varepsilon}}\right) \cdot \Delta\dot{\boldsymbol{\varepsilon}}$ are equivalent to their change caused by strain rate $\Delta\mathbf{D}_{\dot{\boldsymbol{\varepsilon}}}^{\text{vel}}$ and $\Delta\boldsymbol{X}_{\text{s},\dot{\boldsymbol{\varepsilon}}}$ respectively; which is easier to implement than computing the strain-rate derivatives each time step. The Newton–Raphson procedure is detailed in algorithm 3 in Appendix 2.

Substepping algorithm

Once the proportions of elastic and plastic strains have been computed, the viscoplastic stress can be approximated using an explicit modified Euler algorithm with substepping (Sloan *et al*., 2001). In principle, integration follows the same algorithm described in Sloan *et al*. (2001) with minor changes to include the selected viscoplastic framework (i.e. the dashpot or the original consistency–viscoplasticity).

The substepping algorithm (algorithm 4) provides an automatic adequate size of the strain increase. The procedure to subdivide the strain is based on the calculation of the relative error between the two approximations of the increment of stress and state variables ($\Delta\boldsymbol{\sigma}_1$, $\Delta\boldsymbol{\sigma}_2$, $\Delta\boldsymbol{X}_{\text{s},1}$, $\Delta\boldsymbol{X}_{\text{s},2}$) using the modified Euler's algorithm. The step stress and state variables are calculated using equations (34) and (35), respectively.

$$\boldsymbol{\sigma}_{T+\Delta T} = \boldsymbol{\sigma}_0 + 0{\cdot}5(\Delta\boldsymbol{\sigma}_1 + \Delta\boldsymbol{\sigma}_2) \tag{34}$$

$$\boldsymbol{X}_{\text{s},T+\Delta T} = \boldsymbol{X}_{\text{s},0} + 0{\cdot}5\left(\Delta\boldsymbol{X}_{\text{s},1} + \Delta\boldsymbol{X}_{\text{s},2}\right) \tag{35}$$

and the step relative error is calculated using equation (36).

$$R_{T+\Delta T} = \max\left\{\frac{||\Delta\boldsymbol{\sigma}_1 - \Delta\boldsymbol{\sigma}_2||}{2||\boldsymbol{\sigma}_{T+\Delta T}||}, \frac{\left|\left|\Delta\boldsymbol{X}_{\text{s},1} - \Delta\boldsymbol{X}_{\text{s},2}\right|\right|}{2||\boldsymbol{X}_{T+\Delta T}||}\right\} \tag{36}$$

If the relative error is larger than a user-defined tolerance (STOL), the step 'failed', and the increment of strain and strain rate is subdivided using a scaled pseudo-time (ΔT). Sloan *et al*. (2001) propose to calculate the scaling factor (q_R) using equation (37).

$$q_R = 0{\cdot}9\sqrt{\text{STOL}/R_{T+\Delta T}} \tag{37}$$

and subsequently ΔT is updated using $\Delta T \leftarrow q_R\Delta T$.

After the calculation of the updated stress and internal state variables, stress drift can occur (i.e. $\left|F\left(\boldsymbol{\sigma}_{\text{u}}, \boldsymbol{X}_{\text{s,u}}\right)\right| > |\text{FTOL}|$). This drift can be corrected using an algorithm that finds the error in the stress and internal state variables, updating the stress back to the tolerance threshold. The algorithm uses a first-order approximation of the yield function, as shown in equation (38).

$$F \approx F\left(\boldsymbol{\sigma}_0, \boldsymbol{X}_{\text{s},0}\right) + \boldsymbol{n} \cdot \delta\boldsymbol{\sigma} + \boldsymbol{L} \cdot \left(\boldsymbol{a} \cdot \delta\boldsymbol{\varepsilon}^{\text{p}} + \boldsymbol{b} \cdot \delta\dot{\boldsymbol{\varepsilon}}\right) \tag{38}$$

The operator $\delta(\cdot)$ refers to the error in estimating the stress and state variables. In theory, $\delta\dot{\boldsymbol{\varepsilon}} = 0$ because the strain rate is imposed. Therefore, the stress drift correction coincides with the procedure proposed in Sloan *et al*. (2001). Nevertheless, for the original method, the strain-rate error can be computed using $\delta\dot{\boldsymbol{\varepsilon}} = \delta\lambda^{\text{vp}}\boldsymbol{m}/(\Delta t\Delta T)$.

With the considerations described above, the error in the viscoplastic multiplier can be expressed by setting $F = 0$ and

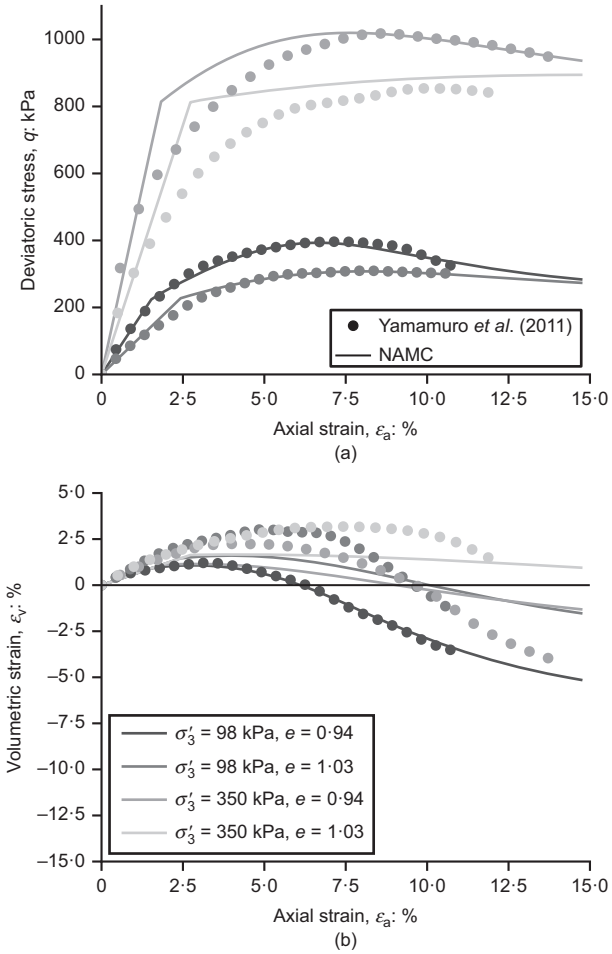

Fig. 10. Comparison between the laboratory data (dots) and the calibrated NAMC at quasi-static strain rate: (a) deviatoric stress plotted against axial strain and (b) volumetric strain plotted against axial strain. The parameters used in the model are summarised in Table 2

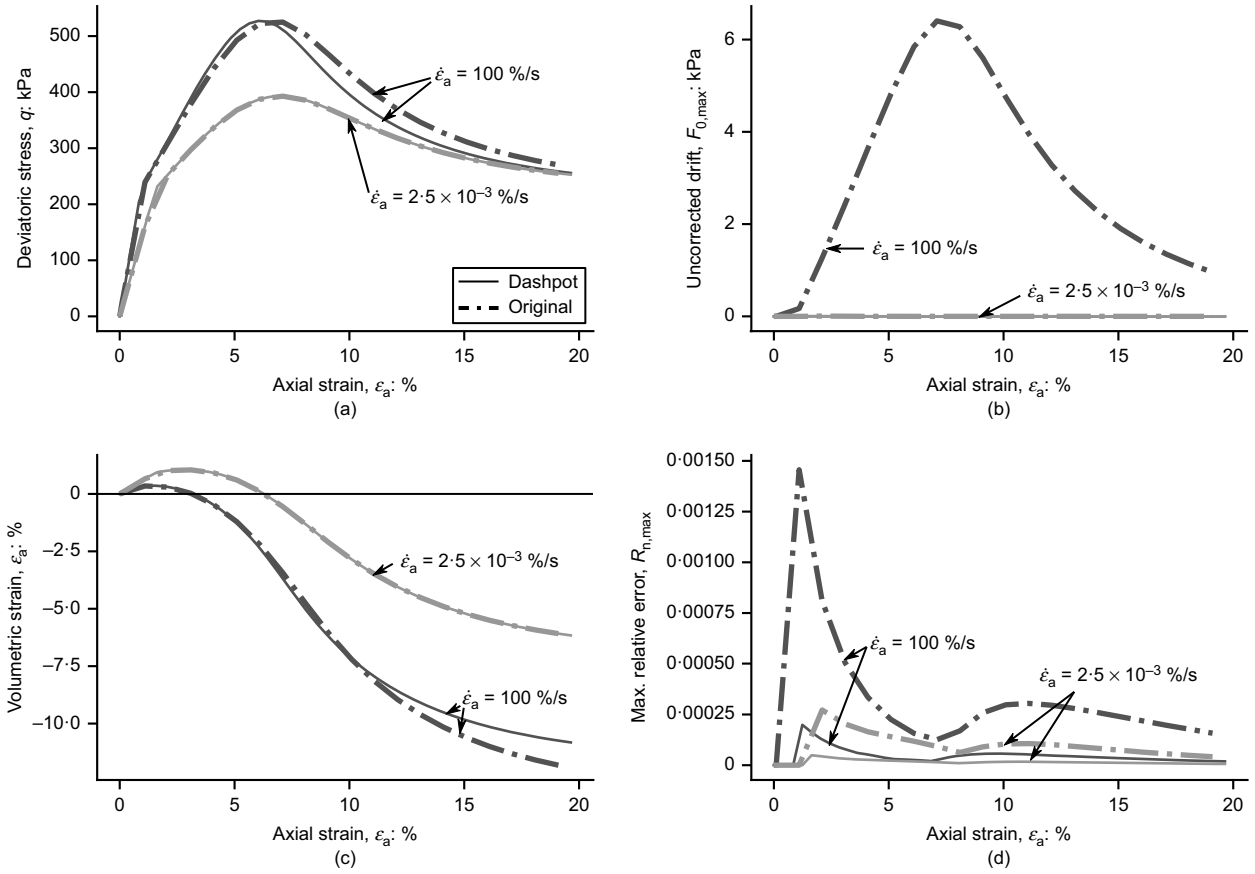

Fig. 11. Comparison between the dashpot (continuous line) and the original (dashed line) viscoplastic integration schemes: (a) deviatoric stress; (b) uncorrected stress drift; (c) volumetric strain; (d) maximum relative residual. All plots have axial strain in the *x*-axis

using the flow rule in equation (16), rendering

$$\delta\lambda^{\mathrm{vp}} = \frac{F_0}{\boldsymbol{n} \cdot \mathbf{D}_0^{\mathrm{vel}} \cdot \boldsymbol{m} + \mathcal{H}^{\mathrm{vp}}} \tag{39}$$

where F_0 is the yield function evaluated at the point where the stresses and state variables are known. Finally, using the flow rule (equation (16)), and the stress–strain relationship (equation (14)) the corrected increments of plastic strain and stress are calculated ($\delta\boldsymbol{\varepsilon}^{\mathrm{p}}$ and $\delta\boldsymbol{\sigma}$). The corrected stresses and state variables are then computed by

$$\boldsymbol{\sigma}_{\mathrm{u}} = \boldsymbol{\sigma}_0 - \delta\boldsymbol{\sigma} \tag{40}$$

$$\boldsymbol{X}_{\mathrm{s}} = \boldsymbol{X}_{\mathrm{s},0} - \delta\boldsymbol{X}_{\mathrm{s}} \tag{41}$$

where $\delta\boldsymbol{X}_{\mathrm{s}}$ can be computed using equation (53). Equations for the NAMC's derivatives $\boldsymbol{a}$, $\boldsymbol{b}$, $\boldsymbol{n}$, $\boldsymbol{m}$ and $\boldsymbol{L}$ are provided in Appendix 1.

RESULTS

Simulations are performed using the IncrementalDriver programme (Niemunis & Grandas-Tavera, 2017). IncrementalDriver is used for single-element tests, in which stress or strain increments can be prescribed and passed to the constitutive model using the Abaqus user-defined material syntax (UMAT). All simulations are performed with $\Delta T_{\min} = 1 \times 10^{-10}$, $\mathrm{STOL} = 1 \times 10^{-3}$ and $\mathrm{FTOL} = 1 \times 10^{-9}$. The discretisation is achieved by subdividing the maximum strain into 1000 steps to achieve the convergence of the prescribed boundary stresses after 200 iterations per step.

First, the model's parameters h and N are calibrated under quasistatic conditions for each test. Subsequently, the results of the dashpot and original viscoplastic approaches are compared in terms of relative error, maximum uncorrected stress drift and computation cost. A comparison between physical and simulated triaxial tests under steady axial strain rate is

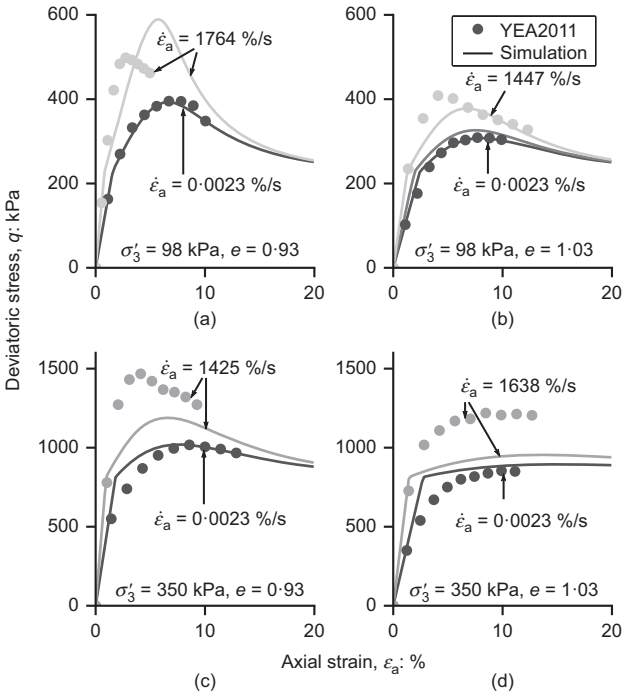

Fig. 12. Deviatoric stress plotted against axial strain curves obtained using κ_D=κ_G=0·04 compared with the YEA2011 data set. The plots are arranged according to initial confinement pressure σ'_3 and initial void ratio e_0: (a) σ'_3 = 98 kPa, e_0 = 0·93; (b) σ'_3 = 98 kPa, e_0 = 1·03; (c) σ'_3 = 350 kPa, e_0 = 0·93; (d) σ'_3 = 350 kPa, e_0 = 1·03

presented. Finally, the model's capacity to reproduce relaxation and pulse testing under transient strain rates is investigated.

Calibration

The hardening modulus h and Nova's coefficient N are calibrated using quasistatic triaxial tests. h and N are chosen by balancing the area below the numerical response and the physical tests using the definition of fitness given in Pal *et al.* (1996). The averaged $M_{tc} = 1{\cdot}31$ is selected with the generally accepted assumption that $M_{tc} = 1{\cdot}31$ should be unique for a specific material. Fig. 10 shows the comparison between physical tests and their numerical counterparts using the calibrated properties shown in Table 2. The experimental stress–strain response is observed to be well captured in all simulations. However, some volumetric strain responses show more dilation than physical tests. This might be due to the

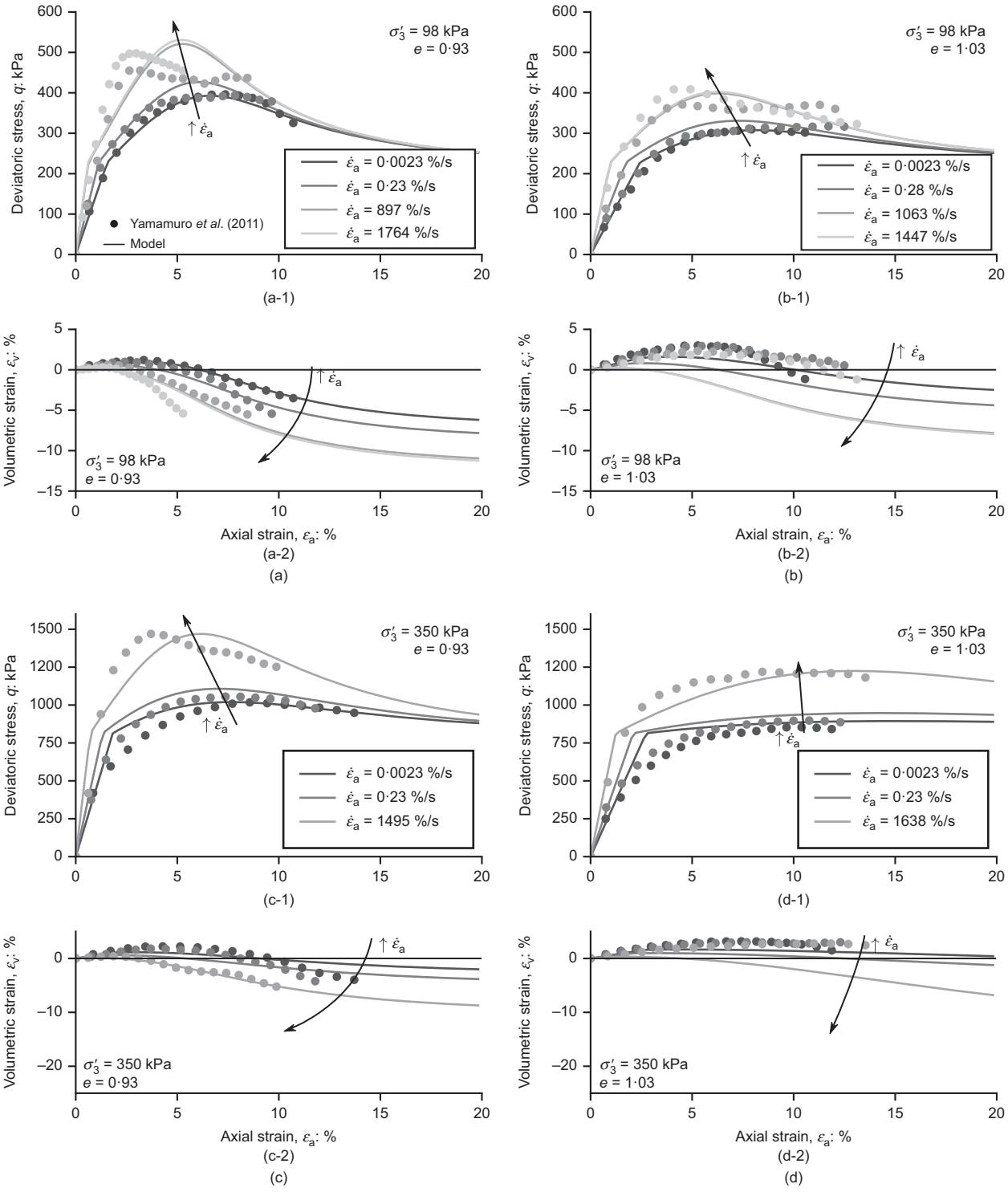

Fig. 13. Comparison between the laboratory drained triaxial tests under HSR in Yamamuro *et al.* (2011) and the simulations using the NAMC for different cell pressures and void ratios: (a-1) deviatoric stress plotted against axial strain, (a-2) volumetric strain plotted against axial strain for $\sigma'_3 = 98$ kPa, $e_0 = 0{\cdot}93$; (b-1) deviatoric stress plotted against axial strain, (b-2) volumetric strain plotted against axial strain for $\sigma'_3 = 98$ kPa, $e_0 = 1{\cdot}03$; (c-1) deviatoric stress plotted against axial strain, (c-2) volumetric strain plotted against axial strain for $\sigma'_3 = 350$ kPa, $e_0 = 0{\cdot}93$; (d-1) deviatoric stress plotted against axial strain, (d-2) volumetric strain plotted against axial strain for $\sigma'_3 = 350$ kPa, $e_0 = 1{\cdot}03$. All simulations are conducted using the dashpot approach

assumption of a unique Poisson's ratio, as mentioned in the viscoplastic NAMC section.

Comparison between the dashpot and original approach

The proposed integration strategies are compared using a triaxial simulation with the same properties as the sample tested at $\sigma_3' = 98$ kPa (Table 2), with $\kappa_D = \kappa_G = 0{\cdot}04$ and $\kappa_K = 2{\cdot}5\kappa_G$ values. The test was simulated at $\dot{\varepsilon}_a = 2{\cdot}5 \times 10^{-3}$ %/s and $\dot{\varepsilon}_a = 100$%/s strain rate. As illustrated in Fig. 11(a), both the original and dashpot integration techniques provide the same solution at low strain rates. However, when the rate and axial strain increase, the original and dashpot approaches diverge (Figs 11(a) and 11(c)). This is also evident in Fig. 11(b), which plots the maximum uncorrected stress drift (F_0, max) against the axial strain. Not surprisingly, the assumption of discarding elastic strain rates unbalances the consistency condition, resulting in the observed drift. A more precise integration technique, such as Runge–Kutta, may be used to resolve the problem mentioned above, although with an increased computational cost.

Similarly, the relative residual error of the modified Euler's procedure (Fig. 11(d)) for the original viscoplasticity approach is higher than the one for the dashpot method. As a result, the dashpot approach is slightly faster than the original (12·1 s to 11·56 s for the simulation shown in Fig. 11). For comparison, the dashpot approach saves around 4·5% of the computation time per integration point.

Apart from the observations made previously, the simulated stiffness and strength also rise when the strain rate increases. Consistently, the material becomes more dative in Fig. 11(c), and the contraction is almost non-existent. This behaviour is further examined in the following section, which employs the model to replicate the YEA2011 data set.

Triaxial tests under constant strain rate

A series of drained triaxial tests are simulated that correspond to the boundary conditions of the tests carried out in Yamamuro *et al*. (2011), with the properties shown in Table 2. The simulations are conducted only with the dashpot approach. Preliminary simulations using constant viscosity coefficients, $\kappa_D = \kappa_G = 0{\cdot}4$ with $\kappa_K = 2{\cdot}5\kappa_G$, resulted in a poor HSR match between YEA2011 and the simulation, as shown in Fig. 12. It is observed that for tests with $\sigma_3' = 98$ kPa, the prediction is closer to the experimental results. In contrast, the maximum deviatoric stress is greatly underestimated for tests with $\sigma_3' = 350$ kPa. Similarly, the results are more underestimated when the material is loose than when it is dense. The variability of the viscosity coefficient κ_D found to fit the YEA2011 data set has been determined and can be summarised in equation (42).

$$\kappa_D = 0{\cdot}0776(1 - D_r) \ln\ (2{\cdot}72\, p'/p_{atm}) \qquad (42)$$

with D_r the relative density and p_{atm} the atmospheric pressure. According to equation (42), as the mean stress increases, the viscosity increases. This relationship indicates a stronger relationship between the grain contacts and the viscoplasticity features observed at HSR.

Figure 13 shows deviatoric stress (q) plotted against axial strain (ε_a) and volumetric strain (ε_v) plotted against axial strain (ε_a). It is observed that the model captures the increase in the peak deviatoric stress and stiffness as the strain rate increases (Figs 13(a-1)–(d-1)). The model captures an early manifestation of peak deviatoric stress, enhanced dilation and less compression, as observed in the subplots of volumetric strain plotted against axial strain (Figs 13(a-2)–(d-2)). The NAMC performs better for dense conditions than for loose conditions, where the model predicts a better fit to both the prediction of deviatoric stress and the prediction of volumetric strain (e.g. Fig. 13(a)). However, one limitation is that the experimental results show a stiffer response in the plastic regime (q_{max} occurs early in the strain domain), indicating a need to increase the hardening modulus with the strain rate. In addition, the q plotted against ε_a curves of simulations with high-strain-rate ratios (i.e. $\dot{\varepsilon}_a/\dot{\varepsilon}_{ref} > 10^5$) seem to coincide. This is because, at high strain rates of similar order of magnitude, equation (11) loses sensitivity (e.g. results of simulations for $\dot{\varepsilon}_a = 897$%/s and $\dot{\varepsilon}_a = 1761$ %/s in Fig. 13(a)).

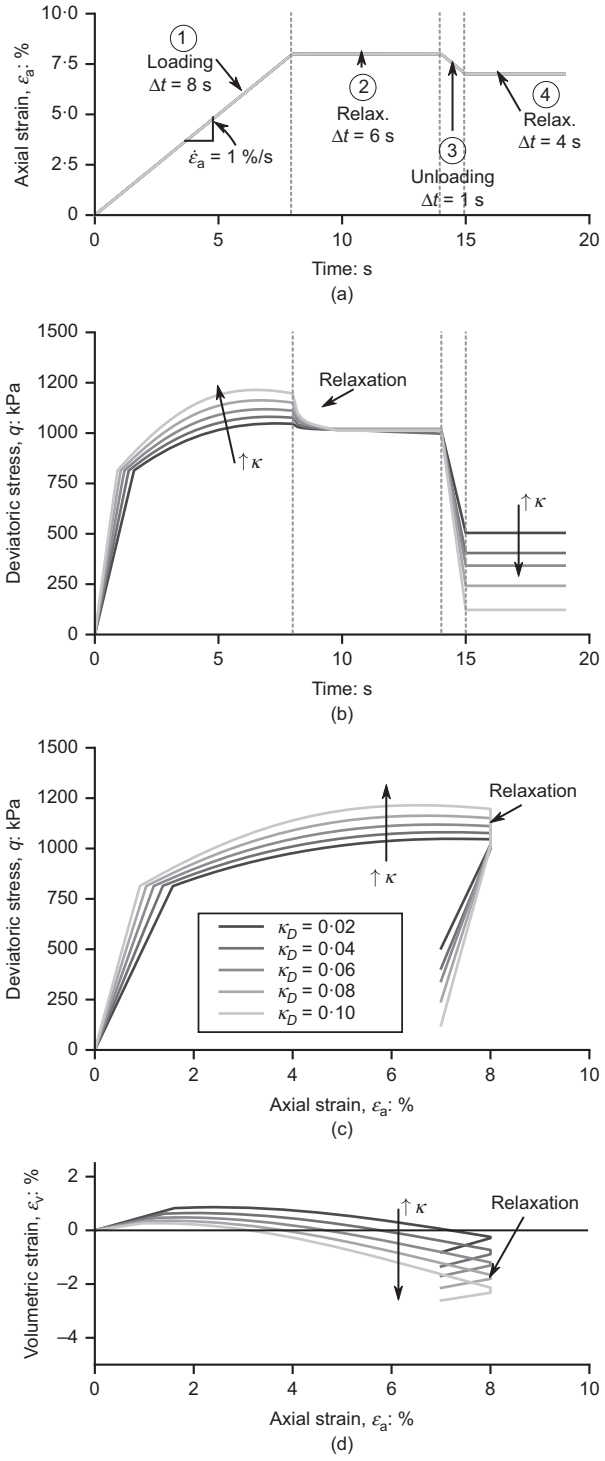

Fig. 14. Simulation of relaxation in a drained triaxial test with σ_3 = 350 kPa: (a) prescribed strain path; (b) deviatoric stress plotted against time; (c) deviatoric stress plotted against axial strain; (d) volumetric plotted against axial strain

Relaxation test

Relaxation tests are conducted to investigate the numerical behaviour of the model for different viscosities κ_D. Five simulations of drained triaxial test are considered with $\sigma_3' = 350$ kPa, the properties in Table 2 and viscosities κ_D ranging from 0·02 to 0·10. The simulations consist of four loading stages (Fig. 14(a)). First, 8% of axial loading is imposed at 1 %/s, after which pure relaxation occurs for 6 s. Subsequently, the sand is unloaded elastically at 1 %/s for 1 s, and finally relaxation occurs for 4 s.

The results of stopping the loading are observed in Figs 14(b)–14(d). As expected, as the viscosity increases, the maximum deviatoric stress increases. However, during the second stage of the simulation, the deviatoric stresses relax and decrease to their quasistatic value independently of their viscosity (Fig. 14(b)). This relaxation is appreciated in the plot of deviatoric stress against axial strain (Fig. 14(c)), in which a vertical drop occurs at constant axial strain, similar to the one-dimensional viscoplastic model of Smith (1960), which is widely used in driven pile applications. During elastic unloading, the model predicts a lower plateau of deviatoric stress, since the modulus increases with the rate of loading. However, there is little effect on the relaxation of stresses in the elastic range during the last stage of the simulation. Finally, as viscosity increases, volumetric dilation also increases (Fig. 14(d)).

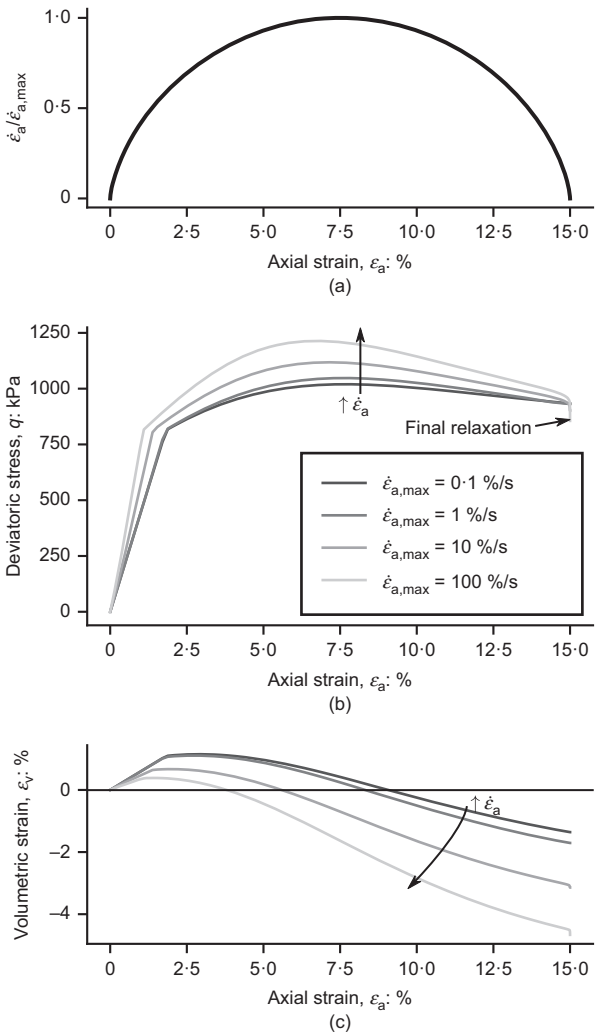

Fig. 15. Results of drained triaxial tests under pulse load for coral sand with σ_3 = 350 kPa and e = 0·94: (a) loading rate; (b) deviatoric stress plotted against axial strain; (c) volumetric strain plotted against axial strain

Pulse loading

A set of drained triaxial tests with the properties presented in Table 2, with $\sigma_3' = 350$ kPa and $e = 0{\cdot}94$ is performed using half the period of a cosine function to simulate the pulse loading shown in Fig. 15(a). The deviatoric stress plotted against axial strain (Fig. 15(b)), and the volumetric strain plotted against axial strain (Fig. 15(c)) responses are similar to their counterparts at constant strain rate (Fig. 13(c)), with the inclusion of a decrease in deviatoric stress due to the strain rate softening process in the last part of the test (Fig. 15(b)). This is because in logarithmic space a sharp reduction of strain rates produces a relaxation effect, manifested as a rapid drop in deviatoric stress at the end of the pulse.

DISCUSSION

Overall, the proposed model captures several features of soil behaviour under HSR that are also reported in models developed with overstress methods (Katona, 1984; An *et al.*, 2011; Higgins *et al.*, 2013; Xu & Zhang, 2015; Mukherjee *et al.*, 2020). A simple NAMC is used with semi-empirical strain-rate hardening/softening equations, which could be used in several applications in geomechanics with minimal calibration effort. In additional, setting $\kappa_K = 2{\cdot}5\kappa_G$ produced acceptable results. Because most geotechnical engineers are familiar with the Mohr–Coulomb model, the implementation of the proposed viscoplastic NAMC in boundary value problems can be expedited. However, the NAMC has limitations owing to its simplicity. For example, NAMC cannot capture plastic deformation under pure volumetric compression, requires individual calibration for different densities, and particle breakage is not considered in the derivation of the model equations.

The YEA2011 data set has limitations due to the difficulties in measuring strains in a highly dynamic triaxial test. Here, it is important to note that volumetric strains were measured locally, which caused distortions in the data that were not feasible to analyse. The reader is directed to Abrantes & Yamamuro (2002) for more information on data acquisition and to Klotz & Coop (2002) for more information on the effect of measuring local strains in defining dilation and the critical state line. Future efforts to extend the experimental data of HSR triaxial testing, whether by physical or discrete-element simulations, are critical in this regard.

A simple power law is selected based on a comparison analysis between the current and some reference values as proposed by equation (8). This functional form, in addition to being simple, captured the trends observed in the data. It provides physical meaning to the viscosity parameter, which can be seen as a damping coefficient. A similar functional form has been selected in other viscoplastic models (Mukherjee *et al.*, 2020). It is also important to highlight that the model lacks sensitivity for strain rates of the same order of magnitude. Further development using the approach in Appendix 1 could be used to construct a more sophisticated model similar to those proposed by Nova & Muir Wood (1982), Jefferies (1993) or Muir Wood (2003).

Finally, the reference strain rate is selected on the basis of the minimum strain rate used in the experiments. More research is required to establish selection criteria. However, a reference strain rate on the order of $\dot{\varepsilon}_{ref} = 2{\cdot}5 \times 10^{-5}$%/s is suggested to start a calibration process, which is equivalent to a typical loading rate in conventional triaxial tests.

CONCLUSIONS

In this study, a simple viscoplastic model based on a non-associated Mohr–Coulomb model is presented.

The model is constructed using Nova's stress–dilatancy equation and through an analysis of the effects of strain rates on the work–energy dissipation. Using the approach above, a strain-rate hardening equation is proposed based on a comparison between the current state variables and the reference or quasistatic state. Besides, it is proposed that the inertial coefficient (I) is used as strain-rate state variable, since it is proportional to $\dot{\varepsilon}_q/\sqrt{p}$. The model equations are calibrated using impact triaxial data sets published in Yamamuro *et al*. (2011) with a good fit between the proposed model and the data.

Two integration approaches based on the enforcement of the consistency equation are presented named: (*a*) the dashpot method (an adaptation of Olszak & Perzyna (1966)) and (*b*) the original consistency method (Wang *et al*., 1997). The theoretical framework is developed and expressed in generic terms so that any inviscid model can be adapted following the proposed numerical implementation contained in Appendix 2.

The following conclusions are drawn from the numerical simulations.

(*a*) Consistency–viscoplasticity offers a reliable alternative to overstress methods. Moreover, since it does not vary significantly from inviscid elasto-plastic models, little effort is required to adapt an inviscid model to form a viscoplastic one.
(*b*) The consistency approach is shown to capture several features of sand behaviour under HSR. For example, the proposed viscoplastic NAMC reproduces increased stiffness under HSR, enhanced maximum deviatoric stress, improved dilation and reduced compression under constant and transient axial strain rates.
(*c*) The original and the dashpot viscoplastic variants yielded comparable results. However, the stress drift for the original method is more significant, necessitating more iterations to correct the drift. Computationally, the dashpot method is slightly superior (at least 4·5% more efficient); however, it may render significantly more rapid and stable solutions in boundary value problems.
(*d*) The consistency–viscoplasticity proposed herein can reproduce relaxation.
(*e*) The calibration against experimental data shows reasonable comparisons; however, more data are needed for various levels of strain rates, confinement, void ratios, mineralogy and particle morphology.

ACKNOWLEDGEMENTS

This material is based in part upon work supported by the National Science Foundation under grant number 1735139. Any opinions, findings and conclusions or recommendations expressed in this material are those of the authors and do not necessarily reflect the views of the National Science Foundation. The authors express their gratitude to the National Science Foundation.

APPENDIX 1. DERIVATION OF EQUATIONS

Work–energy dissipation

The energy balance equation in a continuum medium will now be considered.

$$\dot{W} = \boldsymbol{\sigma} : \dot{\boldsymbol{\varepsilon}} \tag{43}$$

By superposition it is possible to subdivide the inviscid and viscous components of the stress tensor

$$\dot{W} = \left(\boldsymbol{\sigma}^0 + \boldsymbol{\sigma}^{\mathrm{v}}\right) : \dot{\boldsymbol{\varepsilon}} = \boldsymbol{\sigma}^0 : \dot{\boldsymbol{\varepsilon}} + \boldsymbol{\sigma}^{\mathrm{v}} : \dot{\boldsymbol{\varepsilon}} \tag{44}$$

where superscripts $(.)^0$ and $(.)^{\mathrm{v}}$ represent inviscid and viscous components, respectively.

The equation above can be reworked using Roscoe's invariants as in

$$\dot{W} = p\dot{\varepsilon}_{\mathrm{v}} + q\dot{\varepsilon}_q + p^{\mathrm{v}}\dot{\varepsilon}_{\mathrm{v}} + q^{\mathrm{v}}\dot{\varepsilon}_q \tag{45}$$

where the inviscid superscript has been suppressed.

By normalising equation (45) by the mean stress and the deviatoric stress one obtains

$$M = D + \eta + \frac{\left(K^{\mathrm{v}}D^2 + 3G^{\mathrm{v}}\right)}{\sqrt{p}}\frac{\dot{\varepsilon}_q}{\sqrt{p}} \tag{46}$$

with M = critical stress ratio, $\eta = p/q$, $D = \dot{\varepsilon}_{\mathrm{v}}/\dot{\varepsilon}_q$ = dilation, and $\left(K^{\mathrm{v}}D^2 + 3G^{\mathrm{v}}\right)$ an unknown viscoplastic constitutive relationship.

Recall that the inertial coefficient I scales with $1/\sqrt{p}$, and henceforth the unknown terms can be replaced such that, generally

$$M = D + \eta + f(I) \tag{47}$$

with $f(I)$ a linear term of I. Moreover, the normalised change of D is expressed as

$$\frac{\Delta D}{D} \propto \frac{f'(I)\Delta I}{f(I)} \tag{48}$$

For elastic conditions $D^{\mathrm{el}} = G/K$. Integrating equation (48) with limits $G_0/K_0 I \rightarrow I_0$, an equation is obtained of the form

$$\frac{G}{K} = \frac{G_0}{K_0}\left(\frac{I}{I_0}\right)^{\kappa} \tag{49}$$

with κ as a viscosity coefficient. From equation (49) is seen that for G/K to change and produce the behaviour observed in Figs 4 and 5, Poisson's ratio must change. That is only possible if equation (49) is decomposed into

$$\frac{G}{K} = \frac{G_0(I/I_0)^{\kappa_G}}{K_0(I/I_0)^{\kappa_K}} \tag{50}$$

with $\kappa = \kappa_G - \kappa_K$ with $\kappa_K > \kappa_G$ to offset the vertical lines in the stress–dilatancy plot to the left.

By analogy, for the plastic range, the following is obtained

$$D^{\mathrm{p}} = D_0^{\mathrm{p}}\left(\frac{I}{I_0}\right)^{\kappa_D} \tag{51}$$

Consistency equation

The differential of the yield function ($\mathrm{d}F$) can be calculated using a first-order approximation shown in equation (52).

$$\mathrm{d}F = \boldsymbol{n} \cdot \mathrm{d}\boldsymbol{\sigma} + \boldsymbol{L} \cdot \mathrm{d}\boldsymbol{X}_{\mathrm{s}} \tag{52}$$

where $\boldsymbol{n} = \partial F/\partial\boldsymbol{\sigma}$ is a vector normal to the yield surface and $\boldsymbol{L} = \partial F/\partial\boldsymbol{X}_{\mathrm{s}}$ is the direction of maximum change of the yield function with respect to the internal state variables. Similarly, the increment of internal state variables ($\mathrm{d}\boldsymbol{X}_{\mathrm{s}}$) can be calculated with a first-order approximation (equation (53)).

$$\mathrm{d}\boldsymbol{X}_{\mathrm{s}} = \boldsymbol{a} \cdot \mathrm{d}\boldsymbol{\varepsilon}^{\mathrm{vp}} + \boldsymbol{b} \cdot \mathrm{d}\dot{\boldsymbol{\varepsilon}} \tag{53}$$

where $\boldsymbol{a} = \partial\boldsymbol{X}_{\mathrm{s}}/\partial\boldsymbol{\varepsilon}^{\mathrm{vp}}$ is the derivative of the internal state variables with respect to the plastic strain and $\boldsymbol{b} = \partial\boldsymbol{X}_{\mathrm{s}}/\partial\dot{\boldsymbol{\varepsilon}}$ is the derivative of the internal state variables with respect to the strain rate.

Combining equations (52) and (53), the following is obtained

$$\mathrm{d}F = \boldsymbol{n} \cdot \mathrm{d}\boldsymbol{\sigma} + \boldsymbol{L} \cdot \boldsymbol{a} \cdot \mathrm{d}\boldsymbol{\varepsilon}^{\mathrm{vp}} + \boldsymbol{L} \cdot \boldsymbol{b} \cdot \mathrm{d}\dot{\boldsymbol{\varepsilon}} \tag{54}$$

Finally, using equations (14) and (16) as replacements in equation (54), the following is obtained

$$\boldsymbol{n} \cdot \mathbf{D}^{\mathrm{vel}} \cdot \mathrm{d}\boldsymbol{\varepsilon} - \lambda^{\mathrm{vp}}\boldsymbol{n} \cdot \mathbf{D}^{\mathrm{vel}} \cdot \boldsymbol{m} + \lambda^{\mathrm{vp}}\boldsymbol{L} \cdot \boldsymbol{a} \cdot \boldsymbol{m} + \boldsymbol{L} \cdot \boldsymbol{b} \cdot \mathrm{d}\dot{\boldsymbol{\varepsilon}} = 0 \tag{55}$$

Model derivatives

Define $\boldsymbol{X}_{\mathrm{s}} = \{\eta_y(D^{\mathrm{p}})\}$. Thus

$$\boldsymbol{a} = \frac{\partial\boldsymbol{X}_{\mathrm{s}}}{\partial\boldsymbol{\varepsilon}^{\mathrm{vp}}} = \frac{\partial\eta_y}{\partial D^{\mathrm{p}}}\frac{\partial D^{\mathrm{p}}}{\partial\varepsilon_q^{\mathrm{p}}}\frac{\partial\varepsilon_q^{\mathrm{p}}}{\partial\boldsymbol{\varepsilon}^{\mathrm{vp}}} \tag{56}$$

Then, developing the derivatives of the model equations in Table 1

$$\boldsymbol{a} = -(1-N)\left(\frac{I}{I_0}\right)^{\kappa_D} D^{\mathrm{p}}_{\min} h \exp\ (1-h\varepsilon^{\mathrm{p}}_q)\left(1-h\varepsilon^{\mathrm{p}}_q\right)\frac{2\epsilon^{\mathrm{vp}}}{3\varepsilon^{\mathrm{p}}_q} \tag{57}$$

with $\boldsymbol{\epsilon}^{\mathrm{vp}} = \boldsymbol{\varepsilon}^{\mathrm{vp}} - 1/3\varepsilon^{\mathrm{p}}_{\mathrm{v}}\mathbf{1}$ the viscoplastic deviatoric strain tensor.

Similarly

$$\boldsymbol{b} = \frac{\partial \boldsymbol{X}_{\mathrm{s}}}{\partial \dot{\boldsymbol{\varepsilon}}} = \frac{\partial \eta_y}{\partial D^{\mathrm{p}}}\frac{\partial D^{\mathrm{p}}}{\partial I}\frac{\partial I}{\partial \dot{\varepsilon}_q}\frac{\partial \dot{\varepsilon}_q}{\partial \dot{\boldsymbol{\varepsilon}}} \tag{58}$$

Then

$$\boldsymbol{b} = -\frac{\kappa_D}{I_0}(1-N)\left(\frac{I}{I_0}\right)^{\kappa_D - 1} D^{\mathrm{p}}_{\min} h\varepsilon^{\mathrm{p}}_q \exp\ (1-h\varepsilon^{\mathrm{p}}_q)\mathcal{D}\sqrt{\frac{\rho_{\mathrm{s}}}{p'}}\frac{2\dot{\boldsymbol{\epsilon}}}{3\dot{\varepsilon}_q} \tag{59}$$

with $\dot{\boldsymbol{\epsilon}} = \dot{\boldsymbol{\varepsilon}} - 1/3\dot{\varepsilon}_{\mathrm{v}}\mathbf{1}$ the deviatoric strain rate tensor.

For $\mathcal{L}$ there is

$$\mathcal{L} = \frac{\partial F}{\partial \boldsymbol{X}_{\mathrm{s}}} = \frac{\partial F}{\partial \eta_y}$$

Then

$$\mathcal{L} = -p \tag{60}$$

Finally

$$\boldsymbol{n} = \frac{\partial F}{\partial \boldsymbol{\sigma}} = \frac{\partial F}{\partial q}\frac{\partial q}{\partial \boldsymbol{\sigma}} + \frac{\partial F}{\partial p}\frac{\partial p}{\partial \boldsymbol{\sigma}} \tag{61}$$

$$\boldsymbol{m} = \frac{\partial P}{\partial \boldsymbol{\sigma}} = \frac{\partial P}{\partial q}\frac{\partial q}{\partial \boldsymbol{\sigma}} + \frac{\partial P}{\partial p}\frac{\partial p}{\partial \boldsymbol{\sigma}} \tag{62}$$

with

$$\frac{\partial F}{\partial q} = \frac{\partial P}{\partial q} = 1 \tag{63}$$

$$\frac{\partial F}{\partial p} = -\eta_y \tag{64}$$

$$\frac{\partial P}{\partial p} = D^{\mathrm{p}} \tag{65}$$

Finally, $\partial p/\partial\boldsymbol{\sigma}$ and $\partial q/\partial\boldsymbol{\sigma}$ are well-known derivatives.

APPENDIX 2. PSEUDO ALGORITHMS

Algorithm 1: strain-rate threshold

Data: $\dot{\varepsilon}_{q,0}$, $\dot{\varepsilon}_{ref}$, $\dot{\varepsilon}_q$
Result: Boolean and $\Delta\dot{\varepsilon}_q$
begin
  if $\dot{\varepsilon}_{q,0} < \dot{\varepsilon}_{ref} < \dot{\varepsilon}_q$ **then** /* path 1 in Figure 8a */
    Update state and elastic parameters.
    $\Delta\dot{\varepsilon}_q = \dot{\varepsilon}_q - \dot{\varepsilon}_{ref}$
  else if $\dot{\varepsilon}_{q,0} \geq \dot{\varepsilon}_{ref}$, *and* $\dot{\varepsilon}_q \geq \dot{\varepsilon}_{ref}$ **then**/* path 2 in Figure 8a */
    Update state and elastic parameters.
    $\Delta\dot{\varepsilon}_q = \dot{\varepsilon}_q = \dot{\varepsilon}_q - \dot{\varepsilon}_{q,0}$
  else if $\dot{\varepsilon}_{q,0} > \dot{\varepsilon}_{ref} > \dot{\varepsilon}_q$ **then**/* path 3 in Figure 8a */
    Update state and elastic parameters.
    $\Delta\dot{\varepsilon}_q = \dot{\varepsilon}_{ref} - \dot{\varepsilon}_{q,0}$
  else /* Any path in Figure 8b */
    Do not update state nor elastic parameters

Algorithm 2: main REIS algorithm

Data: Δt, $\Delta\boldsymbol{\varepsilon}$, $\boldsymbol{\varepsilon}_0$, $\dot{\boldsymbol{\varepsilon}}_0$, $\boldsymbol{\sigma}_0$, $\boldsymbol{X}_{s,0}$, $\boldsymbol{D}_0^{vel}$
Result: $\boldsymbol{\sigma}$, $\boldsymbol{X}_{s,u}$, $\boldsymbol{D}_u^{vel}$
begin
  Compute $\dot{\boldsymbol{\varepsilon}} = \Delta\boldsymbol{\varepsilon}/\Delta t$;
  Compute strain-rate invariants $\dot{\varepsilon}_{q,0}$ and $\dot{\varepsilon}_q$;
  Store state and elastic parameters:
  $\boldsymbol{D}_u^{vel} \longleftarrow \boldsymbol{D}_0^{vel}$
  $\boldsymbol{X}_{s,u} \longleftarrow \boldsymbol{X}_{s,0}$;
  if *algorithm 1 returns* ***true*** **then**
    for all i and j of the following tensors:
    $D^{vel}_{ik,u} = f_{ik}(D^{el}_{ik,0}, \dot{\varepsilon}_q)$ /* f_{ik} is an updating function */
    $X_{s,iu} = f_i(X_{s,i0}, \dot{\varepsilon}_q)$ /* f_i is an updating function */
  Compute $\Delta\boldsymbol{\sigma}^{vel} = \boldsymbol{D}_u^{vel} \cdot \Delta\boldsymbol{\varepsilon}$;
  if $F(\boldsymbol{\sigma}_0 + \Delta\boldsymbol{\sigma}^{vel},\ \boldsymbol{X}_{s,u}) > FTOL$ **then** /* Plasticity */
    if $(F(\boldsymbol{\sigma}_0,\ \boldsymbol{X}_{s,0}) < -FTOL)$ **then**
      elastoplastic transition find: α with algorithm 3
    else if $F(\boldsymbol{\sigma}_0,\ \boldsymbol{X}_{s,0}) \leq FTOL$ **then**
      Compute β_F with Equation 29;
      if $\beta_F > 90^\circ$ **then**
        elastoplastic unloading use algorithm 3 to compute α
      else
        Pure plasticity $\alpha = 0$
    else
      $F(\boldsymbol{\sigma}_0,\ \boldsymbol{X}_{s,0}) > FTOL \Longrightarrow$ Illegal stress;
      Exit with error
    Compute viscoplastic stresses, strains, and update state parameters using algorithm 4;
    Exit with $\boldsymbol{\sigma}$, $\boldsymbol{X}_{s,u}$, $\boldsymbol{D}_u^{vel}$
  else /* Elasticity */
    Exit with $\boldsymbol{\sigma}$, $\boldsymbol{X}_{s,u}$, $\boldsymbol{D}_u^{vel}$

Algorithm 3: Newton–Raphson algorithm

Data: $\dot{\boldsymbol{\varepsilon}}_0$, $\boldsymbol{\sigma}_0$, $\boldsymbol{X}_{s,0}$, $\boldsymbol{D}_0^{vel}$, $\Delta\boldsymbol{\varepsilon}$, $\Delta\dot{\boldsymbol{\varepsilon}}$,
$\Delta\boldsymbol{D}^{vel}_{\dot{\varepsilon}} = \boldsymbol{D}_u^{vel} - \boldsymbol{D}_0^{vel}$, $\Delta\boldsymbol{X}_{s,\dot{\varepsilon}} = \boldsymbol{X}_{s,u} - \boldsymbol{X}_{s,0}$
Result: α, $\boldsymbol{D}_0^{vel}$, $\boldsymbol{X}_{s,0}$, $\boldsymbol{\sigma}_0$, $\Delta\boldsymbol{\varepsilon}$, $\Delta\dot{\boldsymbol{\varepsilon}}$
begin
  Set $F_0 = F(\boldsymbol{\sigma}_0, \boldsymbol{X}_{s,0})$, $F_T = 100$, $\alpha = 0$, and $n = 0$;
  while $|F_T - F_0| \geq FTOL$ ***and*** $n \leq MAXITER$ **do**
    Store variables:
    $\boldsymbol{D}_\alpha^{vel} \longleftarrow \boldsymbol{D}_0^{vel}$
    $\boldsymbol{X}_{s,\alpha} \longleftarrow \boldsymbol{X}_{s,0}$
    $F_0 \longleftarrow F_T$ and $n \longleftarrow n+1$;
    Compute trial increments:
    $\Delta\boldsymbol{\varepsilon}_\alpha = \alpha\Delta\boldsymbol{\varepsilon}$ and $\Delta\dot{\boldsymbol{\varepsilon}}_\alpha = \alpha\Delta\dot{\boldsymbol{\varepsilon}}$;
    Compute the trial strain rate and its invariants ($\dot{\varepsilon}_{q,\alpha}$):
    $\dot{\boldsymbol{\varepsilon}}_\alpha = \dot{\boldsymbol{\varepsilon}}_0 + \Delta\dot{\boldsymbol{\varepsilon}}_\alpha$;
    if *algorithm 1 returns* ***true*** **then**
      for all i and j of the following tensors:
      $D^{vel}_{ik,\alpha} = f_{ik}(D^{el}_{ik,0}, \dot{\varepsilon}_q)$ /* f_{ik} is an updating function */
      $X_{s,i\alpha} = f_i(X_{s,i0}, \dot{\varepsilon}_q)$ /* f_i is an updating function */
    Update trial stress:
    $\boldsymbol{\sigma}_\alpha = \boldsymbol{\sigma}_0 + \boldsymbol{D}_\alpha^{vel} \cdot \Delta\boldsymbol{\varepsilon}_\alpha$;
    Evaluate F_T, $\boldsymbol{n}$, $\boldsymbol{b}$, and $\boldsymbol{\mathcal{L}}$ on $(\boldsymbol{\sigma}_\alpha, \boldsymbol{X}_{s,\alpha})$;
    Compute F'_α using Equation 33;
    Update α using Equation 32;
  Exit with updated initial parameters:
  α, $\boldsymbol{D}_0^{vel}$, $\boldsymbol{X}_{s,0}$, $\boldsymbol{\sigma}_0$, $\Delta\boldsymbol{\varepsilon}$, $\Delta\dot{\boldsymbol{\varepsilon}}$;

Algorithm 4: substepping algorithm

Data: $\boldsymbol{\sigma}_u$, $\boldsymbol{X}_{s,u}$, $\dot{\boldsymbol{\varepsilon}}_u$, $\Delta\boldsymbol{\varepsilon}$, $\Delta\dot{\boldsymbol{\varepsilon}}$, $\boldsymbol{D}_u^{vel}$
Result: Updated $\boldsymbol{\sigma}_u$, $\boldsymbol{X}_{s,u}$, $\boldsymbol{D}_u^{vel}$
begin
  Set $m = 0$, $T = 0$, $\Delta T = 1$;
  while $T_i 1$ **do**
    Set $\boldsymbol{X}_{s,0} \longleftarrow \boldsymbol{X}_{s,u}$, $\boldsymbol{D}_0^{vel} \longleftarrow \boldsymbol{D}_u^{vel}$, $\boldsymbol{\sigma}_0 \longleftarrow \boldsymbol{\sigma}_u$, $\dot{\boldsymbol{\varepsilon}}_0 \longleftarrow \dot{\boldsymbol{\varepsilon}}_u$;
    Set $\Delta\boldsymbol{\varepsilon}_T \longleftarrow \Delta T\Delta\boldsymbol{\varepsilon}$, $\Delta\dot{\boldsymbol{\varepsilon}}_T \longleftarrow \Delta\dot{\boldsymbol{\varepsilon}}$
    $\dot{\boldsymbol{\varepsilon}}_T = \dot{\boldsymbol{\varepsilon}}_0 + \Delta\dot{\boldsymbol{\varepsilon}}_T$;
    `/* Modified Euler's algorithm begins */`
    for $i = 1 : 2$ **do**
      Compute:
      $\boldsymbol{\sigma}_i = \boldsymbol{\sigma}_{i-1} + (i-1)\Delta\boldsymbol{\sigma}_{i-1}$
      $\boldsymbol{X}_{s,i} = \boldsymbol{\chi}_{s,i-1} + (i-1)\Delta\boldsymbol{X}_{s,i-1}$
      $\dot{\boldsymbol{\varepsilon}}_i = \dot{\boldsymbol{\varepsilon}}_{i-1} + (i-1)\Delta\dot{\boldsymbol{\varepsilon}}_T$;
      if *Algorithm 1 returns* ***true*** **then**
        for all j and k of the following tensors:
        $D_{jk,u}^{vel} = f_{jk}(D_{ik,0}^{el}, \dot{\varepsilon}_q)$
      Compute $\boldsymbol{\sigma}_i^{vel} = \boldsymbol{D}_u^{vel} \cdot \Delta\boldsymbol{\varepsilon}_T$;
      Compute $num = \boldsymbol{n} \cdot \boldsymbol{\sigma}_i^{vel}$ evaluated at $\boldsymbol{\sigma}_i, \boldsymbol{X}_{s,i}, \dot{\boldsymbol{\varepsilon}}_i$;
      if *Algorithm 1 returns* ***true and is dashpot method*** **then**
        Set $num \longleftarrow num + \boldsymbol{\mathcal{L}} \cdot \boldsymbol{b} \cdot \Delta\dot{\boldsymbol{\varepsilon}}_T$ evaluated at $\boldsymbol{\sigma}_i, \boldsymbol{X}_{s,i}, \dot{\boldsymbol{\varepsilon}}_i$
      Compute $Den = \boldsymbol{n} \cdot \boldsymbol{D}_u^{vel} \cdot \boldsymbol{m} + \mathcal{H}$ evaluated at $\boldsymbol{\sigma}_i, \boldsymbol{X}_{s,i}, \dot{\boldsymbol{\varepsilon}}_i$;
      if *Algorithm 1 returns* ***true and is original method*** **then**
        Set $Den \longleftarrow Den - \boldsymbol{\mathcal{L}} \cdot \boldsymbol{b} \cdot \boldsymbol{m}/(\Delta T\Delta t)$ evaluated at $\boldsymbol{\sigma}_i, \boldsymbol{X}_{s,i}, \dot{\boldsymbol{\varepsilon}}_i$
      Compute $\lambda^{vp} = num/Den$;
      Compute $\Delta\boldsymbol{\sigma}_i, \Delta\boldsymbol{X}_{s,i}$ and $\Delta\boldsymbol{\varepsilon}_i^p$ using Equations 14, 53, and 16 respectively;
    `/* Modified Euler's algorithm ends */`
    Compute $\boldsymbol{\sigma}_{T+\Delta T}$ and $\boldsymbol{X}_{s,T+\Delta T}$ using Equations 34 and 35 respectively;
    Compute $R_{T+\Delta T}$ using Equation 36;
    if $R_{T+\Delta T} > STOL$ ***and*** $m \leq MAXSTEPS$ **then**
      $m \longleftarrow m + 1$;
      $q_R = \max\{0.9\sqrt{STOL/R_{T+\Delta T}},\ 0.1\}$;
      Set $\Delta T \longleftarrow \max\{q_R\Delta T, \Delta T_{min}\}$;
      $S_{fail} =$ **True**
    else
      Set $\boldsymbol{D}_u^{vel} \longleftarrow \boldsymbol{D}_{T+\Delta T}^{vel}$, $\boldsymbol{\sigma}_u \longleftarrow \boldsymbol{\sigma}_{T+\Delta T}$, $\boldsymbol{X}_{s,u} \longleftarrow \boldsymbol{X}_{s,T+\Delta T}$, $\dot{\boldsymbol{\varepsilon}}_u \longleftarrow \dot{\boldsymbol{\varepsilon}}_T$;
      `/* Stress drift correction begins */`
      Set $F_c = F(\boldsymbol{\sigma}_0, \boldsymbol{X}_{s,0})$ and $m = 0$;
      while $|F_c| > FTOL$ ***and*** $m \leq MAXITS$ **do**
        Set $F_0 \longleftarrow F_c$ and $m \longleftarrow m + 1$;
        Compute $Den = \boldsymbol{n} \cdot \boldsymbol{D}_0^{vel} \cdot m + \mathcal{H}$ evaluated at $\boldsymbol{\sigma}_0, \boldsymbol{X}_{s,0}, \dot{\boldsymbol{\varepsilon}}_T$;
        if *Algorithm 1 returns* ***true and is original method*** **then**
          Set $Den \longleftarrow Den - \boldsymbol{\mathcal{L}} \cdot \boldsymbol{b} \cdot \boldsymbol{m}/(\Delta T\Delta t)$ evaluated at $\boldsymbol{\sigma}_0, \boldsymbol{X}_{s,0}, \dot{\boldsymbol{\varepsilon}}_T$
        Compute $\delta\lambda^{vp} = F_0/Den$;
        Compute $\boldsymbol{\sigma}_u$ and $\boldsymbol{X}_{s,u}$ using Equations 40 and 41 respectively;
        Evaluate $F_c = F(\boldsymbol{\sigma}_u, \boldsymbol{X}_{s,u})$;
        if $|F_c| > |F_0|$ **then**
          Compute $\delta\lambda^{vp} = F_0/(\boldsymbol{n}^T\boldsymbol{n})$;
          Compute $\boldsymbol{\sigma}_u$ using Equation 40;
          Set $\boldsymbol{X}_{s,u} \longleftarrow \boldsymbol{X}_{s,0}$
        Set $\boldsymbol{\sigma}_0 \longleftarrow \boldsymbol{\sigma}_u$ and $\boldsymbol{X}_{s,0} \longleftarrow \boldsymbol{X}_{s,u}$
      `/* Stress drift correction ends */`
      $q_R = \min\{0.9\sqrt{STOL/R_{T+\Delta T}},\ 1.1\}$;
      if $S_{fail} =$ ***True*** **then**
        $q_R \longleftarrow \min\{q_R, 1\}$;
        $S_{fail} =$ **False**
      Set $\Delta T \longleftarrow q_R\Delta T$ and $T \longleftarrow T + \Delta T$;
      Set $\Delta T \longleftarrow \max\{\Delta T, \Delta T_{min}\}$;
      Set $\Delta T \longleftarrow \min\{\Delta T, 1 - T\}$
  Exit with $\boldsymbol{\sigma}_u$, $\boldsymbol{X}_{s,u}$, $\boldsymbol{D}_u^{vel}$

NOTATION

$\boldsymbol{a} = \partial \boldsymbol{X}_s / \partial \varepsilon^{ep}$	derivative of the internal state parameters with respect to the plastic strain
$\boldsymbol{b} = \partial \boldsymbol{X}_s / \partial \dot{\varepsilon}$	derivative of the internal state variables with respect to the strain rate
$\mathbf{C}^{vp}$	viscoplastic damping matrix
D^p	plastic dilatancy
D^p_{min}	minimum plastic dilatancy
D_r	relative density
$\mathbf{D}^{ep}$	inviscid elastoplastic constitutive matrix
$\mathbf{D}^{vel}$	viscoelastic constitutive matrix
$\mathbf{D}^{vp}$	viscoplastic constitutive matrix
$\mathcal{D}$	particle size
F	yield function
G	shear modulus
$\mathcal{H}$	hardening/softening module
h	hardening parameter
I	inertial coefficient
K	bulk modulus
$\boldsymbol{L} = \partial F / \partial \boldsymbol{X}_s$	direction of maximum change of the yield function with respect to the internal state variables
M	critical stress ratio
M_{tc}	critical stress ratio for triaxial compression
$\boldsymbol{m} = \partial P / \partial \boldsymbol{\sigma}$	vector normal to the plastic potential function
N	Nova's volumetric coupling coefficient
$\boldsymbol{n}$	vector normal to the yield surface
$\boldsymbol{n} = \partial F / \partial \boldsymbol{\sigma}$	vector normal to the yield surface
p'	mean effective stress
p_{atm}	atmospheric pressure
q	deviatoric stress
q_R	substepping scaling factor
$R_{T+\Delta T}$	relative error
$\dot{W}$	rate of internal energy
$\boldsymbol{X}_s$	internal state variables
α	elastic proportion
ΔT	pseudo time step
Δt	time step
β_F	angle between the strain increment and the yield surface normal
$\boldsymbol{\varepsilon}$	strain tensor
$\boldsymbol{\epsilon}$	deviatoric strain tensor
$\dot{\boldsymbol{\varepsilon}}$	strain rate tensor
$\dot{\boldsymbol{\epsilon}}$	deviatoric strain rate tensor
$\dot{\varepsilon}_q$	deviatoric strain rate
ε^p_q	plastic deviatoric strain
$\dot{\varepsilon}_{ref}$	reference strain rate
$\dot{\varepsilon}_v$	volumetric strain rate
ε^p_v	plastic volumetric strain
η	stress ratio
η_y	mobilised stress ratio
κ_D	dilation viscosity
κ_G	shear modulus viscosity
κ_K	bulk modulus viscosity
λ^{vp}	plastic multiplier
ν	Poisson's ratio
ρ_s	solid's density
$\boldsymbol{\sigma}$	stress tensor
σ'_3	effective minor principal stress
$\Phi(F)$	overstress function

OPERATORS

$\mathrm{d}(\cdot)$	differential
$\Delta(\cdot)$	change
$\delta(\cdot)$	error
$\otimes$	tensor product

SUPERSCRIPTS

0	inviscid
ep	inviscid elastoplastic
v	viscous
vel	viscoelastic
vp	viscoplastic

SUBSCRIPTS

0	initial or quasistatic condition
c	critical
u	updated

REFERENCES

Abrantes, A. & Yamamuro, J. (2002). Experimental and data analysis techniques used for high strain rate tests on cohesionless soil. *Geotech. Test. J.* **25**, No. 2, 128, https://doi.org/10.1520/GTJ11356J.

Al-Kafaji, I. K. J. (2013). *Formulation of a dynamic material point method (MPM) for geomechanical problems.* PhD thesis, University of Stuttgart, Stuttgart, Germany, https://doi.org/10.18419/opus-496.

An, J., Tuan, C. Y., Cheeseman, B. A. & Gazonas, G. A. (2011). Simulation of soil behavior under blast loading. *Int. J. Geomech.* **11**, No. 4, 323–334, https://doi.org/10.1061/(ASCE)GM.1943-5622.0000086.

Andrade, J. E., Chen, Q., Le, P. H., Avila, C. F. & Matthew Evans, T. (2012). On the rheology of dilative granular media: bridging solid- and fluid-like behavior. *J. Mech. Phys. Solids* **60**, No. 6, 1122–1136, https://doi.org/10.1016/j.jmps.2012.02.011.

Benson, D. J. (1989). An efficient, accurate, simple ALE method for nonlinear finite element programs. *Comput. Methods Appl. Mech. Engng* **72**, No. 3, 305–350, https://doi.org/10.1016/0045-7825(89)90003-0.

da Cruz, F., Emam, S., Prochnow, M., Roux, J. N. & Chevoir, F. (2005). Rheophysics of dense granular materials : discrete simulation of plane shear flows. *Phys. Rev. E* **72**, No. 2, 021309, https://doi.org/10.1103/PhysRevE.72.021309.

DSS (Dassault Systèmes Simulia) (2012). *ABAQUS Analysis users manual*, Version 6.12. Johnston, RI, USA: Dassault Systèmes Simulia.

Duncan, J. M. & Chang, C. Y. (1970). Nonlinear analysis of stress and strain in soils. *J.Soil Mech. Found. Div.* **96**, No. 5, 1629–1653, https://doi.org/10.1061/JSFEAQ.0001458.

Duvaut, G. & Lions, J. L. (1976). *Les inéquations en mécanique et en physique*, Series Travaux et Recherches Mathematiques, vol. 21. Paris, France: Dunod (in French).

Heeres, O. M., Suiker, A. S. J. & de Borst, R. (2002). A comparison between the Perzyna viscoplastic model and the consistency viscoplastic model. *Eur. J. Mech. – A/Solids* **21**, No. 1, 1–12, https://doi.org/10.1016/S0997-7538(01)01188-3.

Higgins, W., Chakraborty, T. & Basu, D. (2013). A high strain-rate constitutive model for sand and its application in finite-element analysis of tunnels subjected to blast. *Int. J. Numer. Analyt. Methods Geomech.* **37**, No. 15, 2590–2610, https://doi.org/10.1002/nag.2153.

Howard, A. K. (1984). The revised ASTM standard on the unified classification system. *Geotech. Test. J.* **7**, No. 4, 216–222.

Hurley, R. C. & Andrade, J. E. (2015). Friction in inertial granular flows: competition between dilation and grain-scale dissipation rates. *Granul. Matter* **17**, No. 3, 287–295, https://doi.org/10.1007/s10035-015-0564-2.

Jefferies, M. G. (1993). Nor-sand: a simple critical state model for sand. *Géotechnique* **43**, No. 1, 91–103, https://doi.org/10.1680/geot.1993.43.1.91.

Jefferies, M., Been, K. & Been, K. (2015). *Soil liquefaction: a critical state approach*, 2nd edn. Boca Raton, FL, USA: CRC Press, https://doi.org/10.1201/b19114.

Jop, P., Forterre, Y. & Pouliquen, O. (2006). A constitutive law for dense granular flows. *Nature* **441**, No. 7094, 727–730, https://doi.org/10.1038/nature04801.

Katona, M. G. (1984). Evaluation of viscoplastic cap model. *J. Geotech. Engng* **110**, No. 8, 1106–1125, https://doi.org/10.1061/(ASCE)0733-9410(1984)110:8(1106).

Kim, Y., Hossain, M., Wang, D. & Randolph, M. (2015). Numerical investigation of dynamic installation of torpedo anchors in clay. *Ocean Engng* **108**, 820–832, https://doi.org/10.1016/j.oceaneng.2015.08.033.

Klotz, E. U. & Coop, M. R. (2002). On the identification of critical state lines for sands. *Geotech. Test. J.* **25**, No. 3, 289–302.

Lade, P. V., Liggio, C. D. & Nam, J. (2009). Strain rate, creep, and stress drop-creep experiments on crushed coral sand. *J. Geotech. Geoenviron. Engng* **135**, No. 7, 941–953, https://doi.org/10.1061/(ASCE)GT.1943-5606.0000067.

Liingaard, M., Augustesen, A. & Lade, P. V. (2004). Characterization of models for time-dependent behavior of soils. *Int. J. Geomech.* **4**, No. 3, 157–177, https://doi.org/10.1061/(ASCE)1532-3641(2004)4:3(157).

Lu, G. & Fall, M. (2018). State-of-the-art modelling of soil behaviour under blast loading. *Geotech. Geol. Engng* **36**, No. 6, 3331–3355, https://doi.org/10.1007/s10706-018-0560-5.

Muir Wood, D. (2003). *Geotechnical modelling*. Boca Raton, FL, USA: CRC Press.

Mukherjee, M., Gupta, A. & Prashant, A. (2020). A rate-dependent model for sand to predict constitutive response and instability onset. *Acta Geotech.* **16**, 93–111, https://doi.org/10.1007/s11440-020-00988-8.

Niemunis, A. & Grandas-Tavera, C. E. (2017). Computer aided calibration, benchmarking and check-up of constitutive models for soils. Some conclusions for neohypoplasticity. In *Holistic simulation of geotechnical installation processes* (ed. T. Triantafyllidis), Lecture Notes in Applied and Computational Mechanics vol. 82, pp. 168–192. Cham, Switzerland: Springer.

Nova, R. & Muir Wood, D. (1982). A constitutive model for soil under monotonic and cyclic loading. In *Soil mechanics – transient and cyclic loading* (eds G. N. Pande and O. C. Zienkiewicz), pp. 343–373. Chichester, UK: Wiley.

Olszak, W. & Perzyna, P. (1966). The constitutive equations of the flow theory for a non-stationary yield condition. In *Applied mechanics* (ed. H. Görtler), pp. 545–553. Berlin, Germany: Springer.

Omidvar, M., Iskander, M. & Bless, S. (2012). Stress–strain behavior of sand at high strain rates. *Int. J. Impact Engng* **49**, 192–213, https://doi.org/10.1016/j.ijimpeng.2012.03.004.

Pal, S., Wije Wathugala, G. & Kundu, S. (1996). Calibration of a constitutive model using genetic algorithms. *Comput. Geotech.* **19**, No. 4, 325–348, https://doi.org/10.1016/S0266-352X(96)00006-7.

Perzyna, P. (1966). Fundamental problems in viscoplasticity. *Adv. Appl. Mech.* **9**, 243–377, https://doi.org/10.1016/S0065-2156(08)70009-7.

Savitzky, A. & Golay, M. J. (1964). Smoothing and differentiation of data by simplified least squares procedures. *Analyt. Chem.* **36**, No. 8, 1627–1639.

Sloan, S. W., Abbo, A. J. & Sheng, D. (2001). Refined explicit integration of elastoplastic models with automatic error control. *Engng Comput. (Swansea)* **18**, No. 1/2, 121–194, https://doi.org/10.1108/02644400110365842.

Smith, E. A. L. (1960). Pile-driving analysis by the wave equation. *J. Soil Mech. Found. Div., ASCE* **86**, No. 4, 35–64, https://doi.org/10.1061/JSFEAQ.0000281.

Suescun-Florez, E. & Iskander, M. (2017). Effect of fast constant loading rates on the global behavior of sand in triaxial compression. *Geotech. Test. J.* **40**, No. 1, 20150253, https://doi.org/10.1520/GTJ20150253.

Suescun-Florez, E., Omidvar, M., Iskander, M. & Bless, S. (2015). Review of high strain rate testing of granular soils. *Geotech. Test. J.* **38**, No. 4, 511–536.

Sulsky, D., Zhou, S. J. & Schreyer, H. L. (1995). Application of a particle-in-cell method to solid mechanics. *Comput. Phys. Communs* **87**, No. 1–2, 236–252, https://doi.org/10.1016/0010-4655(94)00170-7.

Tran, Q. A. & Soowski, W. (2019). Generalized interpolation material point method modelling of large deformation problems including strain-rate effects application to penetration and progressive failure problems. *Comput. Geotech.* **106**, 249–265, https://doi.org/10.1016/j.compgeo.2018.10.020.

Wang, W. M., Sluys, L. J. & Borst, R. D. (1997). Viscoplasticity for instabilities due to strain softening and strain-rate softening. *Int. J. Numer. Methods Engng* **40**, No. 20, 3839–3864, https://doi.org/10.1002/(SICI)1097-0207(19971030)40:20<3839::AID-NME245>3.0.CO;2-6.

Xu, T. & Zhang, L. (2015). Numerical implementation of a bounding surface plasticity model for sand under high strain-rate loadings in LS-DYNA. *Comput. Geotech.* **66**, 203–218, https://doi.org/10.1016/j.compgeo.2015.02.002.

Yamamuro, J. A., Abrantes, A. E. & Lade, P. V. (2011). Effect of strain rate on the stress–strain behavior of sand. *J. Geotech. Geoenviron. Engng* **137**, No. 12, 1169–1178, https://doi.org/10.1061/(ASCE)GT.1943-5606.0000542.

Yerro Colom, A. (2015). *MPM modelling of landslides in brittle and unsaturated soils.* PhD thesis, Universitat Politecnica de Catalunya, Barcelona, Spain.

Zambrano-Cruzatty, L. E. (2021). *Advancements for the numerical simulation of free fall penetrometers and the analysis of wind erosion of sands.* PhD thesis, Virginia Polytechnic Institute and State University, Blacksburg, VA, USA.

Zambrano-Cruzatty, L. & Yerro, A. (2020). Numerical simulation of a free fall penetrometer deployment using the material point method. *Soils Found.* **60**, No. 3, 668–682, https://doi.org/10.1016/j.sandf.2020.04.002.